



## Dust plumes over the Pacific, Indian, and Atlantic oceans: Climatology and radiative impact

Aihua Zhu,<sup>1</sup> V. Ramanathan,<sup>1</sup> Fang Li,<sup>1</sup> and Dohyeong Kim<sup>1</sup>

Received 17 January 2007; revised 28 March 2007; accepted 11 June 2007; published 31 August 2007.

[1] Multiple satellite data sets in conjunction with the Monte Carlo Aerosol-Cloud-Radiation (MACR) model are employed to determine climatological distributions and radiative impacts of dust plumes over the Pacific, Indian, and Atlantic oceans. Three target regions, namely the Yellow Sea (YS), Arabian Sea (AS), and Saharan Coast (SC), are examined for quantitative comparisons of dust properties and their impacts on climate. Twenty year averaged Advanced Very High Resolution Radiometer (AVHRR) aerosol optical depth (AOD) data clearly show the peak dust season for the three target regions, March–April–May for YS and June–July–August for AS and SC. Georgia Institute of Technology–Goddard Global Ozone Chemistry Aerosol Radiation and Transport (GOCART) modeled dust AOD fraction and Moderate Imaging Spectroradiometer (MODIS) large-mode AOD ratio are adopted to evaluate the dust fraction estimate. Stratospheric Aerosol and Gas Experiment (SAGE) II aerosol extinction coefficient data are used to define the vertical distribution of dust. The elevated dust plumes are detected by subtracting the non-dust-season values from dust season values of SAGE II data, showing extinction peak around  $\sim 4$  km over AS and SC. Over YS, dust plumes are found presenting multilayered structure. The shortwave (SW) forcing of dust, although moderated by the longwave (LW) effect, dominates the net effects (SW + LW) of dust plumes. Under clear-sky (i.e., cloudless) conditions, dust plumes reduce about  $5.9 \text{ W m}^{-2}$ ,  $17.8 \text{ W m}^{-2}$ , and  $14.2 \text{ W m}^{-2}$  regional and seasonal mean radiative flux reaching the surface over YS, AS, and SC, respectively. Of the three regions, dust plumes over AS have the largest effect on atmospheric heating owing to a lower single-scattering albedo and the relatively large dust loading. The maximum SW heating occurs over AS with the value around  $+0.5 \text{ K/day}$  inside the dust layer at  $\sim 4$  km. The LW effect results in strong cooling throughout the dust layer and moderate heating below the dust layer, and dust plumes over SC exert the maximum LW effect on heating rates, with up to  $-0.5 \text{ K/day}$  LW cooling in the free troposphere and about  $+0.3 \text{ K/day}$  warming in the boundary layer. As the sum of the SW and the LW heating rates, net heating rate shows a more complex pattern. Over SC, large LW cooling inside the dust layer offsets up to 80% SW heating and results in about  $-0.1 \text{ K/day}$  net heating rate change at the height  $\sim 5$  km over SC. Over AS the net heating rate change is dominated by SW heating because the maximum LW cooling is less than 60% of the SW heating, which leads to  $+0.3 \text{ K/day}$  net heating inside the dust layer and moderate heating below the dust base. The net heating rate change over YS is the smallest among the three regions, with magnitude within  $0.1 \text{ K/day}$ .

**Citation:** Zhu, A., V. Ramanathan, F. Li, and D. Kim (2007), Dust plumes over the Pacific, Indian, and Atlantic oceans: Climatology and radiative impact, *J. Geophys. Res.*, *112*, D16208, doi:10.1029/2007JD008427.

### 1. Introduction

[2] Airborne dust aerosols have been documented extensively [Harrison *et al.*, 2001; Duce, 1995; Mahowald *et al.*, 2006]. The dominance of dust aerosols over anthropogenic

aerosols was shown by Li and Ramanathan [2002], e.g., for the Arabian Sea, the authors showed that the summer time (June–July–August) aerosol optical depth (AOD) (mainly due to dust) far exceeded the dry season anthropogenic aerosol AODs. Of increasing interest is the climate impact introduced by dust aerosols through regulation of the radiation budget [IPCC, 2001]. Dust aerosols, the silicate particles suspending in the atmosphere, cut down incoming solar radiation reaching the surface via reflection and absorption. Moreover, dust particles also interact with LW

<sup>1</sup>Center for Clouds, Chemistry and Climate (C<sup>4</sup>), Scripps Institution of Oceanography, University of California, San Diego, La Jolla, California, USA.

flux mainly through the absorption of the outgoing LW radiation originating from the underlying regions. The aforementioned effects are the so-called direct radiative forcing of dust aerosols. On the other hand, acting as cloud condensation nuclei (CCN) and ice nuclei, dust particles may modify the albedo and lifetime of clouds [Twomey, 1977; DeMott *et al.*, 2003; Sassen *et al.*, 2003], defined as the first and second indirect effect, respectively. The additional heating induced by mineral dust can also lead to reduction of liquid water path and cloud cover [Huang *et al.*, 2006], causing a semidirect effect. The strong radiative forcing by dust aerosols may further lead to potential impacts to the regional climate and hydrological cycle. The model simulation by Lau *et al.* [2006] indicated that the mixture of dust aerosols and soot can heat the air over the Tibetan Plateau, which may alter the Asian monsoon circulation.

[3] By parameterization of mineral dust within the Hadley Centre atmospheric general circulation model (AGCM), Woodward [2001] yielded a global annual mean direct dust radiative forcing of  $+0.07 \text{ W m}^{-2}$  at the top of the atmosphere (TOA), and  $-0.82 \text{ W m}^{-2}$  at the surface. However, the peak forcing introduced by dust aerosol can be up to 2 orders of magnitude larger than the global annual mean values, especially downstream of the dust source regions such as the Saharan Desert, Taklamakan Desert, Gobi Desert, and Arabian Desert and so on. The largest and most persistent dust sources are found to be mainly in the Northern Hemisphere extending from north Africa, Middle East, central and south Asia, and China [Prospero *et al.*, 2002]. Inside this broad “dust belt”, three distinct dust plumes over the oceans can be distinguished, which are east Asian dust plume over the North Pacific Ocean in the spring time, Saharan dust plume over the Atlantic Ocean and the Arabian dust plume over the Indian Ocean [Li and Ramanathan, 2002] during the summer months. Although, impressive progress has been achieved in the development of numerical aerosol models to simulate the emission, deflation, transport, and deposition of atmospheric aerosols on regional and global scales [Penner *et al.*, 2001; Woodward, 2001; Perlwitz *et al.*, 2001; Song and Carmichael, 2001; Gong *et al.*, 2003; Shao *et al.*, 2003; Chin *et al.*, 2002; Zender *et al.*, 2003], very few models were able to adequately predict dust optical depth when compared with the observations [Sokolik *et al.*, 2001; Lunt and Valdes, 2002]. The deficiency of numerical models to accurately simulate the dust optical depth necessitates the comprehensive use of all kinds of observations for the study of dust radiative forcing.

[4] Various field experiments have been conducted to study the physical and chemical characteristics and radiative impacts of dust aerosols. These include the 2nd Aerosol Characterization Experiment (ACE-2) [Raes *et al.*, 2000], the Puerto Rico Dust Experiment (PRIDE) [Colarco *et al.*, 2003a, 2003b], the Saharan Dust Experiment (SHADE) [Haywood *et al.*, 2003; Tanré *et al.*, 2003; Myhre *et al.*, 2003], Aeolian Dust Experiment on Climate impacts (ADEC) [Shi *et al.*, 2005], and ACE-Asia [Seinfeld *et al.*, 2004]. However, the systematic comparison of climatology and radiative effects of the aforementioned three major dust plumes have never been done before owing to limited observations and scarce data. With the advantages of

advanced techniques to monitor large-scale atmospheric aerosols over long periods, satellite data help to fill the gap of insufficient observations and significantly improve our understanding of the behaviors of dust plumes [Kaufman *et al.*, 2005; Husar *et al.*, 2001]. Li *et al.* [2004] provided an observationally constrained shortwave radiative forcing of Saharan dust by employing Moderate Imaging Spectroradiometer (MODIS) AOD and the Clouds and the Earth’s Radiant Energy System (CERES) flux data. These successful achievements encourage us to apply more satellite data to study the climatology and radiative impacts of dust plumes over the global oceans.

[5] In this study, we will focus on the climatology and radiative impacts of three major dust plumes over the Northern Hemisphere: the east Asian dust plume over the Pacific Ocean, the Arabian dust plume over the Indian Ocean, and the Saharan dust plume over the Atlantic Ocean. For this purpose, five different satellite data sets were combined. Providing the longest observation period (1981–2001), National Oceanic and Atmospheric Administration (NOAA) Pathfinder Advanced Very High Resolution Radiometer (AVHRR) aerosol data are appropriate for the analysis of temporal and spatial climatology of dust plumes. SAGE II aerosol extinction coefficient data are used to determine the vertical distribution of dust plumes. MODIS large-mode AOD data and aerosol model results derived from GOCART [Chin *et al.*, 2002; Ginoux *et al.*, 2001] were used to evaluate the dust fraction estimate. Total Ozone Mapping Spectrometer (TOMS) and Multiangle Imaging Spectroradiometer (MISR) AOD data are employed to examine the consistency among different satellite observations. MODIS level-2 AOD data are applied to Monte Carlo Aerosol-Cloud-Radiation (MACR) model to assess the direct radiative forcing, and atmospheric heating rate change introduced by mineral dust. The single-scattering albedo measured at Aerosol Robotic Network (AERONET) [Holben *et al.*, 1998] dust-dominated sites and refractive index observed by previous experiments near upstream source regions are employed to represent the optical properties of dust particles.

[6] Section 2 describes the radiative transfer model, satellite aerosol products and other input parameters employed in this study. The climatological results of dust plumes derived from satellite data are presented in section 3. The radiative impacts induced by dust plumes are shown in section 4, followed by section 5 with discussion about the uncertainties and limitations of this study. Conclusions are summarized in section 6.

## 2. Model and Data

[7] The MACR radiative transfer model, satellite-derived aerosol data, and other input parameters employed in this study are discussed in this section.

### 2.1. Radiative Transfer Model

[8] Monte Carlo Aerosol-Cloud-Radiation (MACR) model is adopted to evaluate the climate impacts introduced by dust aerosols. MACR was first developed at the Center for Clouds, Chemistry and Climate (C<sup>4</sup>), Scripps Institution of Oceanography during the Indian Ocean Experiment (INDOEX) [Ramanathan *et al.*, 2001; Podgorny and

Ramanathan, 2001; Podgorny *et al.*, 1998; Satheesh *et al.*, 1999; Vogelmann *et al.*, 2001]. Using the Maximum Cross-Section Method [Marchuk *et al.*, 1980], MACR computes the photon transport in the media and estimates the radiative flux at each interface. In the current version, a total of 32 SW bands (from 0.25  $\mu\text{m}$  to 5.0  $\mu\text{m}$ ) and 16 LW bands (from 3.0  $\mu\text{m}$  to 1000.0  $\mu\text{m}$ ) are used for the solar and terrestrial radiation calculations, respectively. MACR can treat the scattering, absorbing, and emission by gases, clouds, and aerosols. Clouds are classified into low, middle, and high clouds (on the basis of their height), as well as convective clouds. To account for the gaseous absorption, the updated gas absorption database HITRAN2000 [Rothman *et al.*, 2003] and CKD2.4 [Clough *et al.*, 1989] for water vapor continuum are incorporated with the correlated- $k$  distribution method [Goody *et al.*, 1989; Fu and Liou, 1992; Lacis and Oinas, 1991; Kato *et al.*, 1999], which includes up to 20 correlated- $k$  coefficients at each band. The absorptions of water vapor, ozone, carbon dioxide, and oxygen are considered in both SW and LW portions. Trace gases, such as  $\text{CH}_4$ ,  $\text{N}_2\text{O}$ , and CO are also contained in the LW absorption calculation.

## 2.2. Satellite-Derived Aerosol Data

### 2.2.1. AVHRR

[9] Recognizing the need to improve long time series data sets for global change research, NOAA and NASA initiated the “Early Earth Observing System (EOS) Pathfinder Data Set Activity” in 1990. The Pathfinder Program focuses on how the existing satellite data sets could be processed and used to study global change. The long time series data sets are applied to the stable calibrations and community consensus algorithms [Stowe *et al.*, 1997]. AVHRR Pathfinder atmospheric data sets cover the period from June 1981 to July 2001 and use a quasi-equal area grid (equivalent to the area of a  $1^\circ$  latitude/longitude grid box at the equator  $\sim 110$  km by 110 km) for the computation of statistics and the storage of mapped data. The aerosol retrieval algorithm is based on a simple Junge aerosol size distribution (size parameter,  $v = 3.5$ ) for the nonabsorbing aerosols (real part of refractive index is 1.5) [Stowe *et al.*, 1997]. AOD is estimated from backscattering radiation measured at an effective wavelength of 0.63  $\mu\text{m}$  for cloud-free days (2nd generation) over the dark oceans (surface reflectance  $\sim 1.5\%$ ). Cloud screening procedures are based on the fact that the cloud reflectance is high and relatively constant for the most visible and infrared spectrums. In contrast, aerosol backscattering is much stronger in the visible than in the near and far infrared range. Pixels containing clouds can be identified and removed by comparing the observed signal in near-IR with that in the absence of clouds. This cloud screening approach cannot retrieve AOD when its value is larger than 2.0 because the separation between cloud and aerosol becomes ambiguous for remote sensing when AOD exceeds this value [Stowe *et al.*, 2002]. With the longest observation period, AVHRR aerosol products are expected to provide the most complete climatological descriptions on the spatial and temporal variations of dust plumes.

### 2.2.2. MODIS

[10] MODIS aerosol products present the ambient AOD over the oceans globally and over a portion of the continents with low surface albedo. There are two MODIS aerosol data

sets: One contains data from the Terra platform, and another collects data from the Aqua platform. In this study we chose Terra data, because the observations period exceeds that of the Aqua data by 2 years. Daily Level-2 AOD data are produced at the spatial resolution of a 10 by 10 km (at nadir) pixel array. The observed TOA reflectance at seven wavelengths (0.47, 0.55, 0.66, 0.87, 1.24, 1.64, and 2.13  $\mu\text{m}$ ) was compared to a precomputed look-up table, which contains the reflectance for an array of angles, size distributions and optical depths [Tanré *et al.*, 1997]. The modeled reflectance with the smallest difference from the observed reflectance is retrieved from the look-up table. This best fit reflectance is associated with a corresponding set of aerosol properties. Currently, nine tropospheric aerosol models are used, including four small-mode models and five large-mode models. The scattering and absorbing properties are derived from the analyses of AERONET data and LANDSAT Thematic Mapper (TM) images [Tanré *et al.*, 2001; Kaufman *et al.*, 2001]. Aerosol size information is currently derived for ocean areas only. MODIS cloud mask determination combines both SW and LW channels for a total of 13 channels. Additional cloud screening with regard to the neighboring pixels is also considered in the algorithm after the application of cloud mask. Because cirrus cloud can be highly transparent and contaminate the retrieval of aerosol product, MODIS cloud screening algorithm subtracts cirrus effect by rejecting 25–33% of the brightest and darkest pixels at 865 nm within the 10 by 10 km box [Martins *et al.*, 2002]. The low-reflectance pixels of small signal-to-noise ratio are also excluded to maintain the quality of the results (Y. J. Kaufman and D. Tanré, Algorithm for remote sensing of tropospheric aerosol from MODIS, 1998, available at [http://modis.gsfc.nasa.gov/data/atbd/atbd\\_mod02.pdf](http://modis.gsfc.nasa.gov/data/atbd/atbd_mod02.pdf)). MODIS AOD data from 2000 to 2004 are used to estimate the optical depths of dust particles, and applied to the MACR radiative model to assess the radiative impacts of dust plumes.

### 2.2.3. TOMS and MISR

[11] TOMS AOD record covers the periods from January 1979 to April 1993 (Nimbus7-TOMS observations), and from July 1996 to December 2000 (Earth Probe TOMS measurements). These data sets are tabulated on a  $1^\circ$  by  $1^\circ$  grid between  $89.5^\circ\text{S}$  and  $89.5^\circ\text{N}$ . The backscattered radiances ( $I_\lambda$ ) measured at two wavelengths  $\lambda_1$  and  $\lambda_2$  are used in the aerosol retrieval algorithm, which is based on the theoretical framework presented by Torres *et al.* [1998]. Particles are characterized by comparing measured and precomputed spectral contrast ( $I_{\lambda_1}/I_{\lambda_2}$ ) and the radiance at the longer wavelength ( $I_{\lambda_2}$ ). Wavelength pairs at 340 and 380 nm are used for Nimbus 7 data and pairs at 331 and 360 nm are for the Earth Probe TOMS data. In this study the Earth Probe TOMS monthly averaged data sets are used because of its good quality control [Torres *et al.*, 2002]. The MISR instrument orbits the Earth about 15 times each day and accomplishes the nearly global coverage within 9 days. MISR collects multiangle as well as multispectral data, which are not available from any other satellite instruments. Viewing the sunlit Earth simultaneously at nine widely spaced angles ( $0$ – $70.5^\circ$ ), MISR provides radiometrically and geometrically calibrated images in four spectral bands (446, 558, 672, and 866 nm) at each angle. With this particular ability, MISR can retrieve AOD over land with

**Table 1.** Single-Scattering Albedo, Asymmetry Factor, and Ångström Exponent at 550 nm for Yellow Sea (Dunhuang), Arabian Sea (Solar Village), and Saharan Coast (Cape Verde) From Aerosol Robotic Network Dust-Dominated Sites

Parameter	YS	AS	SC
SSA	0.964	0.933	0.948
ASY	0.745	0.680	0.690
ANG	0.299	0.410	0.360

a bright surface [Diner *et al.*, 2001]. Three years of MISR AOD data (2000–2002) are analyzed in this study. TOMS and MISR AOD data are employed to examine the consistency of different satellite AOD data sets.

#### 2.2.4. SAGE II

[12] The SAGE II sensor was launched into a 57° inclination orbit aboard the Earth Radiation Budget Satellite (ERBS) in October 1984. During each sunrise and sunset encountered by the orbiting spacecraft, the instrument uses the solar occultation technique measuring the attenuated solar radiation through the Earth's limb in seven channels with central wavelengths ranging from 0.385 to 1.02  $\mu\text{m}$ . The transmittance measurements are inverted using the “onion-peeling” approach [Antuña *et al.*, 2002] to retrieve the aerosol extinction coefficient ( $\text{km}^{-1}$ ) as well as the other atmospheric compounds such as ozone, nitrogen dioxide, and water vapor at 0.385, 0.453, 0.525, and 1.02  $\mu\text{m}$ . These data, in conjunction with data from sister instruments SAM II and SAGE I, can be used to estimate long-term constituent trends and to identify responses to episodic events. SAGE II has a horizontal resolution of the order of 200 km and a vertical resolution of 1 km [Kent *et al.*, 1998]. A global climatology of stratospheric aerosol radiative properties has been compiled from SAGE II multiwavelength extinction measurements [Thomason *et al.*, 1997]. Although SAGE II was initially designed for detecting stratospheric aerosols, its 1.02  $\mu\text{m}$  aerosol extinction coefficient profiles have actually been retrieved reaching down to the boundary layer [Wang *et al.*, 1999; Thomason and Taha, 2003; Kent *et al.*, 2003]. Sufficient tropospheric data have been accumulated under cloudless conditions after long observation period. These low-level SAGE II data afford a rough but potential way to understand the vertical distributions of tropospheric aerosols. In this study, aerosol extinction coefficient data ( $\text{km}^{-1}$ ) at 1.02  $\mu\text{m}$  was used because of its better quality [Kent *et al.*, 1998].

#### 2.3. Other Input Parameters for MACR

[13] Three important optical parameters are required in order to estimate direct radiative forcing by spherical aerosol particles using the MACR model, which are single-scattering albedo (SSA), asymmetry factor (ASY), and Ångström exponent (ANG). Because of the variety of the mineralogical compositions, dust particles from different regions show quite different optical properties [Sokolik and Toon, 1999]. To compare the radiative forcing due to the dust particle itself, the optical properties of dust particle sampled near the source regions are considered only. For example, we select aerosol optical properties from desert site upwind of China to model YS dust. For SW calculation, SSA, ASY, and ANG data are derived from three dust-dominated AERONET sites [Dubovik *et al.*, 2002; Eck *et al.*,

2005], which are Dunhuang (40°N, 94°E) for the North Pacific Ocean, Solar Village (24°N, 46°E) for the Indian Ocean, and Cape Verde (16°N, 22°W) for the North Atlantic Ocean. As shown in Table 1, dust in Arabian Sea is most absorbing among three regions, with SSA at 550 nm to be 0.933, while dust in Yellow Sea is more scattering. For LW radiative forcing consideration, the field sampled refractive index data near the Taklamakan Desert [Shi *et al.*, 2005], Afghanistan [Sokolik *et al.*, 1993], and Barbados [Volz, 1973] were employed to represent the dust aerosols over the North Pacific Ocean, the Indian Ocean, and the North Atlantic Ocean. These refractive index data, as shown in Figure 1, were applied to MIE code by assuming the lognormal distribution (mode radius is 0.5  $\mu\text{m}$ , standard deviation is 2.0) to consider the spectral variation of SSA in the LW spectrum. It is clearly seen that at around 9  $\mu\text{m}$ , Saharan dust shows the largest absorption (Figure 1a, the imaginary part of the refractive index) among the three regions, suggesting strong absorption of LW flux by Saharan dust [Volz, 1973].

[14] The monthly mean temperature, specific humidity, surface wind, and geopotential height derived from the ECMWF ERA-40 [Uppala *et al.*, 2005] reanalysis data (1981–2001) are used to describe the state of the atmo-

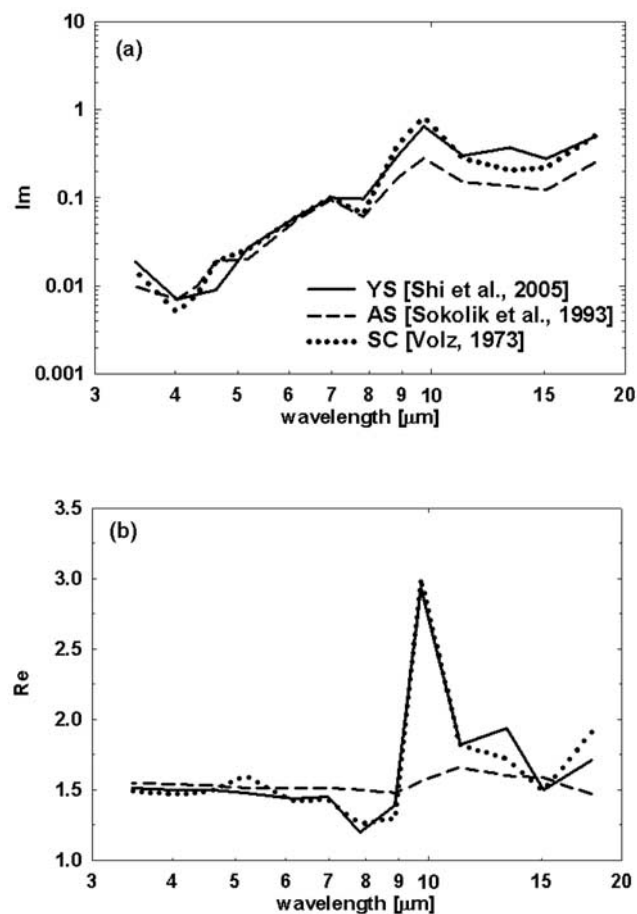


**Figure 1.** Spectral variation of (a) imaginary part and (b) real part of dust refractive index for Yellow Sea (YS, from Shi *et al.* [2005]), Arabian Sea (AS, from Sokolik *et al.* [1993]), and Saharan Coast (SC, from Volz [1973]).

sphere. The NOAA OI-2 SST data (1971–2000) [Reynolds *et al.*, 2002] are employed to estimate IR emissions from the ocean surface. For the cloud fraction and optical depth, 15 types of International Satellite Cloud Climatology Project (ISCCP)–D2 monthly mean cloud products (1984–2000) are combined into four cloud types: low, middle, high, and deep convective clouds [Rossow and Schiffer, 1999; Rossow *et al.*, 1996; Chung *et al.*, 2005].

### 3. Climatological Results

[15] Climatological results derived from the aforementioned satellite data are presented in this section. The seasonal variation, spatial distribution, the dust fraction relative to total AOD, and dust vertical profile are described for the dust plumes over the Pacific, Indian, and Atlantic oceans.

#### 3.1. Seasonal Variation

[16] The spatial and temporal distributions of 20-year averaged (1981–2001) AVHRR AOD (630 nm) are shown as a function of longitude over the North Pacific Ocean (latitude range: 30°N–50°N) (Figure 2a), as a function of latitude over the Indian Ocean (longitude range 50°E–70°E) (Figure 2b), and as a function of longitude over the North Atlantic Ocean (latitude range 5°N–25°N) (Figure 2c). The high aerosol loading and maximum transport across the oceans can be seen clearly in March–April–May (MAM) over the North Pacific and in June–July–August (JJA) over both the Indian and the North Atlantic oceans. During other seasons, although high AOD exists near the coast, the transport of aerosols is limited and AOD is usually less than 0.15 in the remote oceans.

[17] The annual cycle of the aerosol plumes derived from long term AVHRR AOD data is consistent with the acknowledged dust seasons in previous studies. On the basis of 49 years (1949–2002) daily observed data from 681 national meteorological stations in northern China, Zhou and Zhang [2003] demonstrated that the frequency of severe dust storms in spring accounts for more than 80% in the whole year. The study by Chun and Lim [2004] also confirms that spring is the season with the most frequent east Asian dust storms over Korea. On the basis of the surface observations, Ackerman and Cox [1989] showed the annual peak of dust outbreaks over Arabian regions from late spring to early fall. Li and Ramanathan [2002] reported similar findings by utilizing satellite data with winds field from surface to 500mb. The study by Prospero and Carlson [1981] as well as Mbourou *et al.* [1997] pointed out that the greatest dust concentrations occur in the summer months at Barbados, and trade winds can transport Saharan dusts to the Caribbean cross the Atlantic when the Intertropical Convergence Zone (ITCZ) moves northward in summer. In our study, dust seasons are defined to be boreal spring (MAM) for the Pacific and JJA for the Indian and Atlantic oceans.

#### 3.2. Regional Distribution

[18] In Figure 3, seasonal mean spatial distributions of 20-year averaged AVHRR AOD (630 nm) are shown for the dust season only over the Pacific Ocean (MAM), Indian Ocean (JJA), and Atlantic Ocean (JJA). The geographic

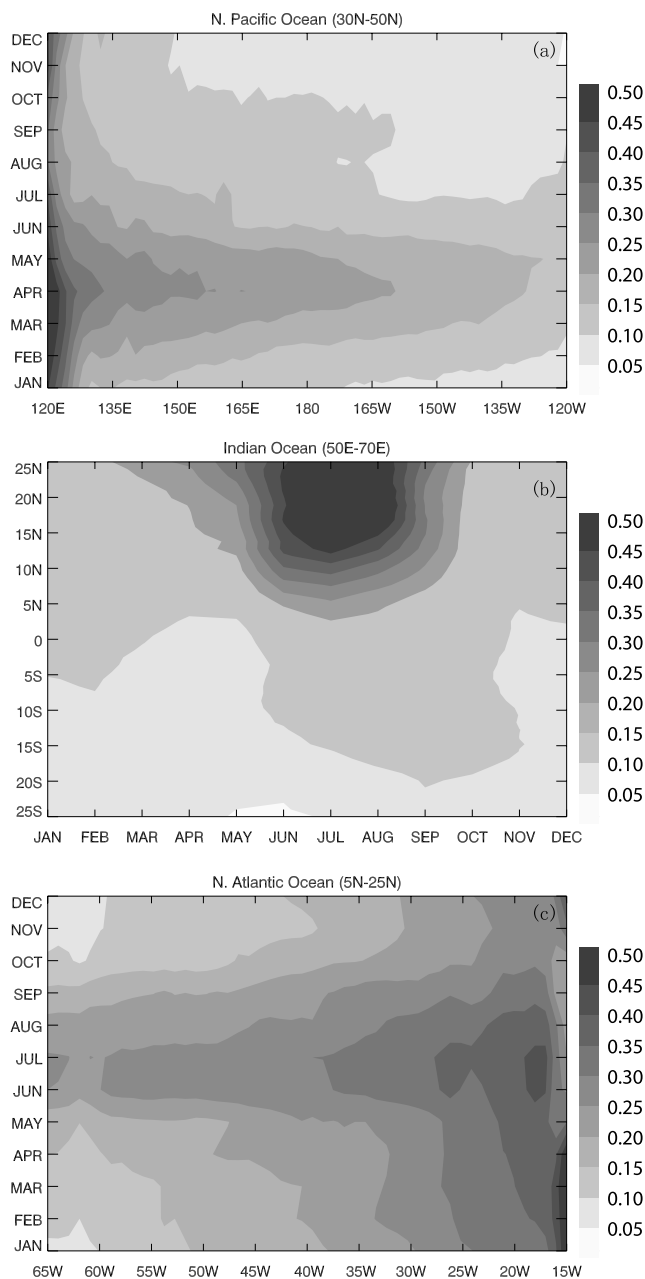


**Figure 2.** Spatial and temporal distributions of 20-year averaged (1981–2001) Advanced Very High Resolution Radiometer (AVHRR) aerosol optical depth (AOD) (630 nm) (a) as a function of longitude over the North Pacific Ocean (latitude range: 30°N–50°N), (b) as a function of latitude over the Indian Ocean (longitude range 50°E–70°E), and (c) as a function of longitude over the North Atlantic Ocean (latitude range 5°N–25°N).

distribution of dust plumes has been demonstrated clearly, with high AOD close to the continental coast line and gradually declining with distance away from the source. Large amounts of dust particles are removed from the atmosphere during long-range transport cross the ocean sectors, resulting in large AOD gradients from the source to the remote ocean.

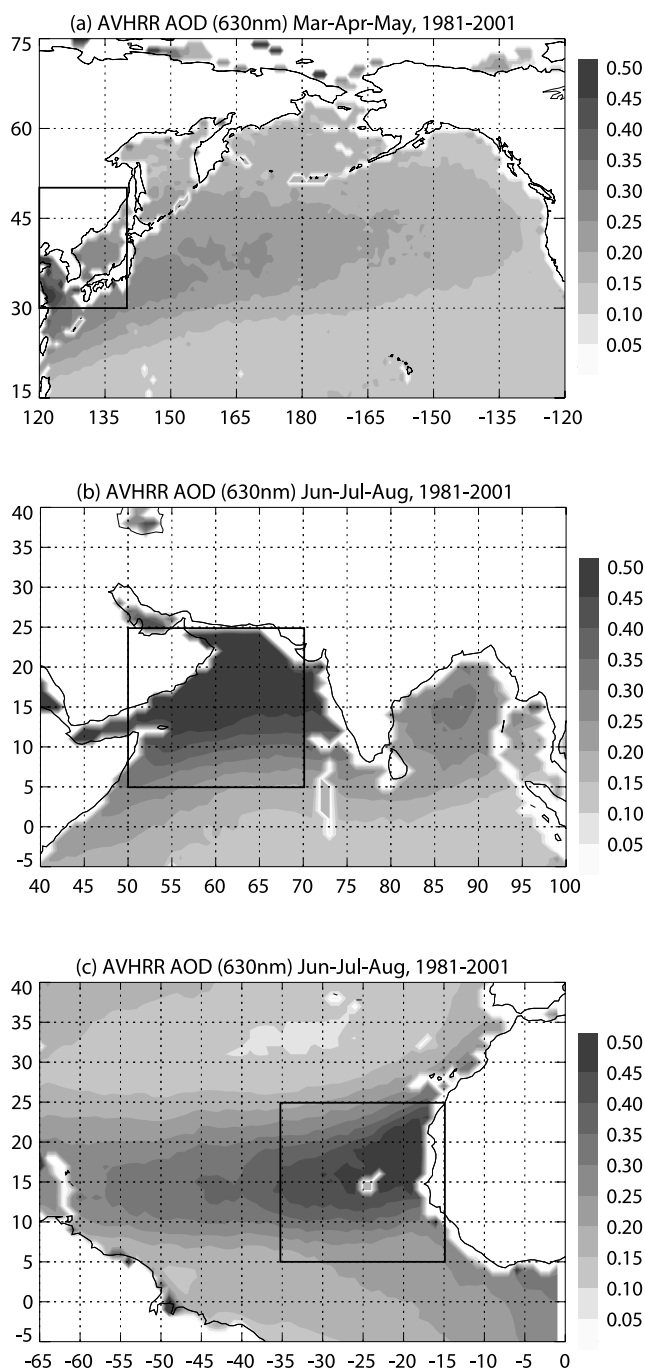


**Figure 3.** Seasonal mean AVHRR AOD (630 nm) (averaged from 1981 to 2001) over the (a) Pacific Ocean (MAM), (b) Indian Ocean (JJA), and (c) Atlantic Ocean (JJA). Target area ( $20^\circ$  by  $20^\circ$ ) is marked by the black box.

[19] By means of the long term National Centers for Environmental Prediction/National Center for Atmospheric Research (NCEP/NCAR) wind fields, *Li and Ramanathan* [2002] found that the long range transport patterns of the dust plumes are mainly determined by the prevailing winds over each ocean sector. With the assistance of the strong midlatitude westerlies, the Pacific dust plume (Figure 3a) is transported northeastward across the Pacific Ocean and can reach as far as the West Coast of North America, where

AOD is still as high as  $\sim 0.15$ . The southward spread of the dust plume from Arabian and Indian continent can reach to as south as  $5^\circ\text{N}$  with AOD larger than 0.2 (Figure 3b), although the prevailing wind is southwesterly during the well-known Indian summer monsoon season. This southwest winds not only blow the clean maritime air toward the continent, might also carry dust particles from Somalia to the Arabian Sea. The extremely high AOD ( $>0.6$ ) over the Arabian Sea is also caused by dust aerosols originating from the Arabian Peninsular, transported by the strong northwesterly offshore wind [*Pease et al.*, 1998], which is one branch of the cyclonic flow with low-pressure center over the Asian mainland owing to strong surface heating in the summer time [*Sirocko*, 1991]. The westward transport of dust plume over the North Atlantic Ocean (Figure 3c) is assisted by the equatorial trade winds when the ITCZ moves northward in the summer; however, this transport is mainly confined in the narrow band between  $10^\circ\text{N}$  and  $20^\circ\text{N}$  because of both the geographic distribution of dust sources and the prevailing wind belt.

[20] To quantitatively compare the dust plumes, three target areas (marked by the black box in Figure 3) with same areas ( $20^\circ$  by  $20^\circ$ ) are selected as the Yellow Sea (YS,  $30^\circ\text{N}$ – $50^\circ\text{N}$ ,  $120^\circ\text{E}$ – $140^\circ\text{E}$ ) in the North Pacific Ocean, the Arabian Sea (AS,  $5^\circ\text{N}$ – $25^\circ\text{N}$ ,  $50^\circ\text{E}$ – $70^\circ\text{E}$ ) in the Indian Ocean, and the Saharan Coast (SC,  $5^\circ\text{N}$ – $25^\circ\text{N}$ ,  $15^\circ\text{W}$ – $35^\circ\text{W}$ ) in the eastern Atlantic Ocean. The results hereafter were retrieved for the target areas only.

### 3.3. AOD Consistency Among Different Spacecraft Observations

[21] The assessment of the accuracy of AOD products from different satellite data sets is a prerequisite to an analysis of dust radiative impacts. MODIS AOD has been validated with the ground-based AERONET observations with mixed results [*Remer et al.*, 2002; *Chu et al.*, 2002; *Ichoku et al.*, 2002; *Chung et al.*, 2005]. While instantaneous MODIS values compare well with AERONET, monthly mean values have biases of about 0.05 in certain regions [*Remer et al.*, 2002]. In this study, we examine the consistency of different AOD data sets derived by AVHRR, TOMS, MISR, and MODIS. Since each AOD data set has been retrieved at its specific wavelength, i.e., 630 nm for AVHRR, 380 nm for TOMS, 558 nm for MISR, and 550 nm for MODIS, MODIS Ångström exponent data were employed to interpolate AOD from different wavelength to an identical wavelength 550 nm for the comparison. Figure 4 shows the comparison of AOD at 550 nm among four satellite data sets from January 1997 to December 2004. All of the data sets reveal similar seasonal cycle and clearly show AOD peak during the boreal summer (JJA) over AS and SC, and in the spring time (MAM) over YS.

[22] Quantitative comparisons using MODIS AOD as the reference are shown in Table 2 over the three regions. It shows that AVHRR AOD is smaller than MODIS AOD over all three regions, with the bias ranging from a negligible  $-0.003$  over AS to  $-0.087$  over YS, which might comes from the idealized assumption of nonabsorbing aerosols in the retrieval algorithm of AVHRR. For TOMS and MISR, the results are dependent on regions, since both produce smaller AOD over YS, while larger AOD over AS and SC. The fairly small root-mean-square (RMS) error

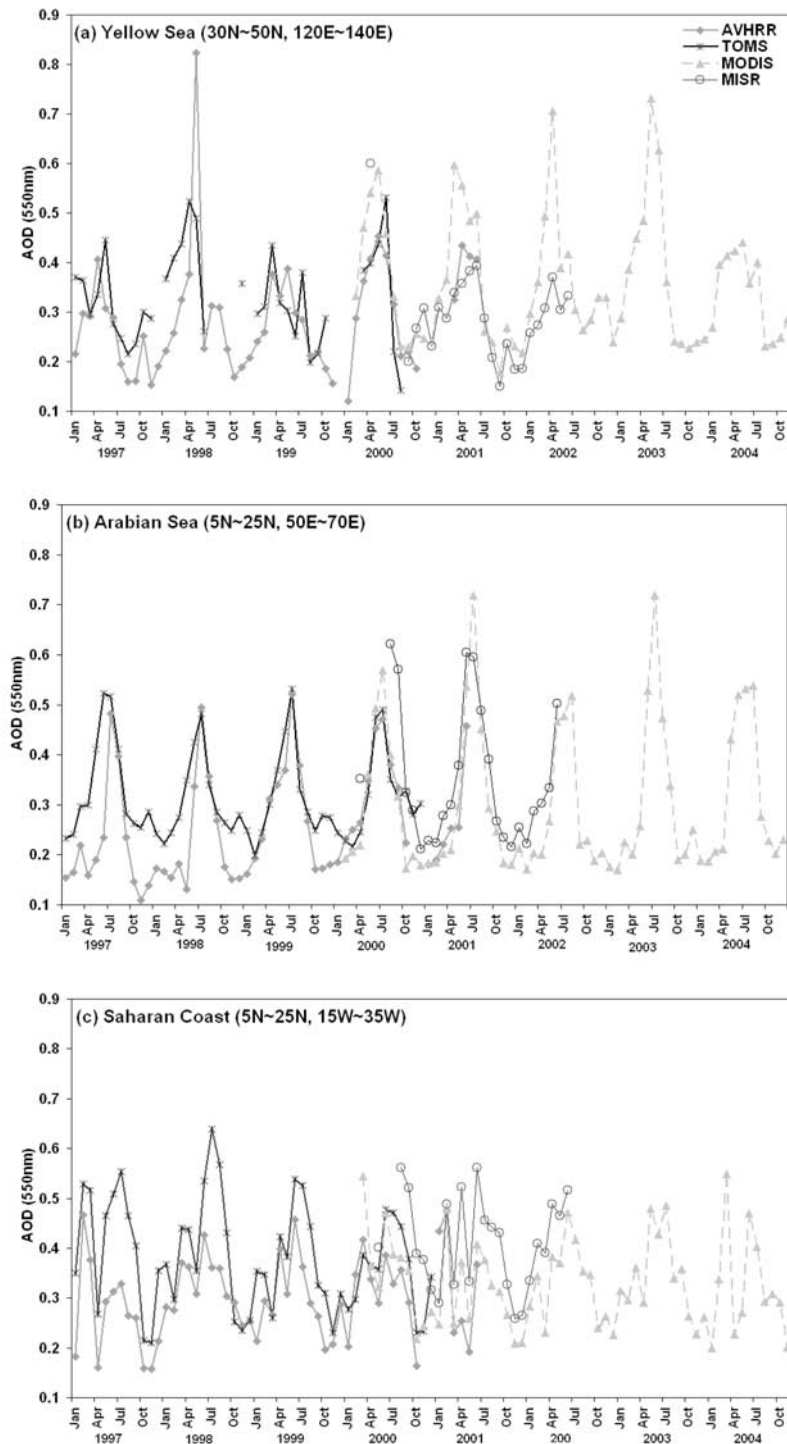


**Figure 4.** Consistencies of AOD (550 nm) from AVHRR, Total Ozone Mapping Spectrometer (TOMS), Multiangle Imaging Spectroradiometer (MISR), and Moderate Imaging Spectroradiometer (MODIS) data set over (a) YS, (b) AS, and (c) SC.

confirms the consistency among different satellite data sets and supports our approach of employing AVHRR AOD data for the study of dust plume climatology.

### 3.4. Dust Fraction

[23] One major advantage of the MODIS aerosol data set is the detailed information of particle-size-related aerosol

optical properties, i.e., small-mode AOD and large-mode AOD [Tanré *et al.*, 1997]. The ratio of large or small-mode AOD to total AOD highlights the importance of particle size and can help distinguish the dominance between natural aerosol (mainly coarse-mode aerosol) and manmade aerosol (primarily small mode) [Remer *et al.*, 2002]. The recent

**Table 2.** Mean Aerosol Optical Depth Difference Between Moderate Imaging Spectroradiometer (MODIS) and Advanced Very High Resolution Radiometer, Total Ozone Mapping Spectrometer, and Multiangle Imaging Spectroradiometer Over Yellow Sea, Arabian Sea, and Saharan Coast<sup>a</sup>

Data Sets	Region		
	Yellow Sea	Arabian Sea	Saharan Coast
AVHRR-MODIS	-0.087 (0.068)	-0.003 (0.045)	-0.038 (0.071)
TOMS-MODIS	-0.084 (0.074)	+0.022 (0.070)	+0.012 (0.065)
MISR-MODIS	-0.071 (0.094)	+0.074 (0.070)	+0.095 (0.048)

<sup>a</sup>The values in parenthesis represent root-mean-square error.

research by *Bellouin et al.* [2005] employed MODIS small-mode AOD to estimate the global annual mean direct radiative forcing by anthropogenic aerosols. In our study, MODIS large-mode AOD data are used to estimate the fraction of dust particles relative to total aerosols, which is further compared with GOCART model results to test its ability for the estimation of dust fraction.

[24] Figure 5 shows monthly variation of MODIS large-mode AOD ratio over YS, AS, and SC averaged from 2000 to 2004. The error bar, representing the 5-year averaged standard deviation of the ratio in each month is defined as

$$err = \frac{\sum_{j=2000}^{2004} E_j}{5}, \quad \text{where } E_j = \sqrt{\frac{\sum_{i=1}^N (x_i - \bar{x})^2}{N-1}}, \quad (1)$$

$x_i$  is the ratio at  $i$  grid in  $j$  year,  $\bar{x}$  is the regional mean ratio in the investigating region,  $N$  is the total number of grids with available data. It is clearly seen in Figure 5 that large-mode AOD ratios seldom exceed 50% over all the three regions throughout most of the months, implying relatively large contributions of fine-mode aerosols, which are mainly composed of anthropogenic aerosols. Clear seasonal cycles of the large-mode AOD ratio can be seen over YS and AS, with minimum large-mode ratio over YS during summer while maximum over AS the same period. Over SC, however, the large-mode ratio shows very small annual variations, implying relatively persistent and stable sources for coarse-mode aerosols. The lowest large-mode ratio (<40%) and the greatest error bar ( $\sim\pm 30\%$ ) are found over YS, which suggests the complex nature of aerosol components and varying emission of coarse aerosol particles at that region.

[25] Although MODIS large-mode AOD ratio can be used to estimate the fraction of coarse particles, it has large uncertainty to represent the whole contribution of mineral dust because sea salt aerosols are unavoidably included in the large-mode aerosols over the oceanic region, while some dust particles with small size might be excluded from the large-mode AOD ratio. To validate MODIS large-mode ratio, GOCART model results are used to derive the dust AOD fraction during dust season and compared with MODIS large-mode ratio. Owing to the limited availability of GOCART model results, dust fractions from GOCART are only shown for the year 2001 (Figure 6). It is clearly seen that MODIS large-mode ratio is much smaller than GOCART dust fraction over SC (Figure 6c), and the

maximum dust fraction estimated by GOCART is over 80% in June, while MODIS large-mode ratio is less than 50%. Even though MODIS large-mode ratios are close to GOCART dust fractions over YS and AS (Figures 6a and 6b), if the contribution of sea salt aerosols are subtracted from MODIS large-mode AOD ratio the dust contribution estimated by MODIS large-mode ratio will become smaller than GOCART values. The seasonal mean MODIS large-mode AOD ratios are 32%, 50%, and 48% for YS, AS, and SC, respectively, while 29%, 54%, and 77% from GOCART dust fractions for each corresponding region.

[26] Another possible uncertainty of dust fraction estimated by the MODIS large-mode ratio is the exclusion of fine-mode dust particles. Fine-mode dust particles were found to account for large amount of total dust optical depths [*d'Almeida and Schütz*, 1983; *Duce*, 1995]. To demonstrate the possible contribution of fine-mode dust particles to total AOD, AERONET fine-mode AOD fraction measured near the desert source regions are investigated. The fine-mode AOD fraction during dust season (MAM) accounts for about 25% of total AOD at Dunhuang site, which is close to the major dust source region ( $\sim 550$  km east of the Taklamakan Desert basin). Similar results can be found over other AERONET dust-dominated sites. For example, during summer time, the fine-mode AOD fractions at Solar Village and Cape Verde are 37% and 27%, respectively. The large value of fine-mode AOD fraction over the AERONET dust-dominated sites during the dust season implies that fine-mode dust particles might also have large contribution to total dust optical depth.

[27] In view of the obvious deficiency to distinguish sea salt from large dust particles, and to extract the small size dust particles from fine-mode aerosols, MODIS large-mode AOD ratio might cause large uncertainty to estimate dust AOD fraction. Without more sophisticated observations, dust fraction from the model is probably the only way to estimate the optical depth by dust aerosols only. However, the reliability of GOCART 1 year model result might lead to some errors to the radiative forcing calculations, which will be discussed with details in section 5. In this study, the

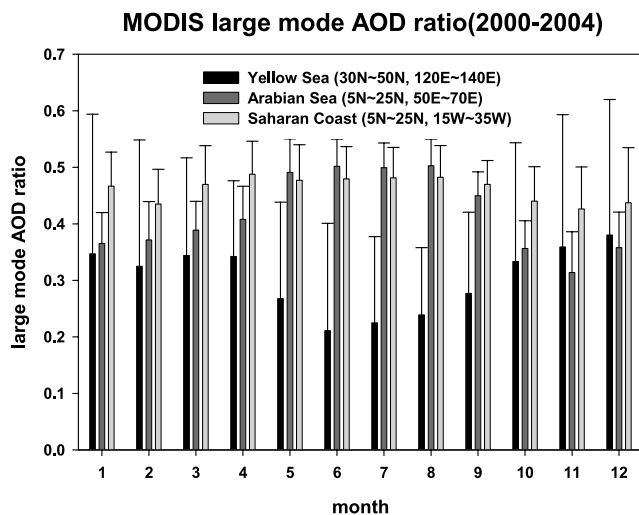


**Figure 5.** MODIS large-mode AOD ratio over YS, AS, and SC averaged from 2000 to 2004.

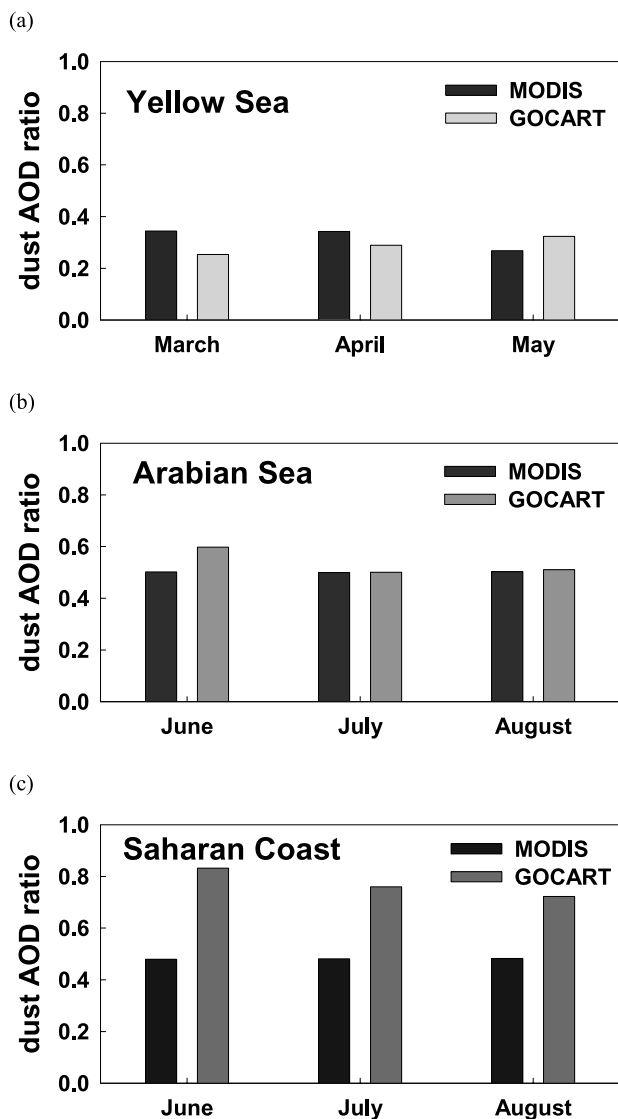


**Figure 6.** Comparison between MODIS large-mode AOD ratio (2000–2004) and GOCART (2001) dust fraction during the dust season over (a) YS, (b) AS, and (c) SC.

seasonal averaged GOCART dust AOD fractions are used to estimate the contribution of dust particles.

### 3.5. Vertical Profile

#### 3.5.1. Method and Results

[28] The vertical distribution of dust plume is one of the critical parameters in the assessment of dust radiative forcing [Claquin *et al.*, 1998]. The model study by Carlson and Benjamin [1980] showed that the atmospheric heating rate can be changed dramatically by the elevated Saharan dust layer. Liao and Seinfeld [1998] claimed that clear-sky LW forcing and cloudy-sky TOA SW forcing are very sensitive to the altitude of the dust layer. Meloni *et al.* [2005] pointed out that SW aerosol radiative forcing at TOA had a strong dependence on aerosol vertical profiles. SAGE II aerosol extinction coefficient data ( $\text{km}^{-1}$ ) provide a potential way to estimate the vertical structure of dust plumes. During the observation period of SAGE II from 1984 to 2001, there were several major volcanic eruptions,

such as El Chichon in 1982 and Pinatubo in 1991, which may contaminate the real signal of tropospheric aerosols. To avoid the influences of volcanic aerosols, the aerosol profiles during volcanic years were excluded.

[29] The averaged aerosol profiles during the dust season (MAM for YS, JJA for AS and SC) are shown by the solid lines in Figure 7. For the comparison, the aerosol profiles during the non-dust-season, which is the remaining 9 months of the year, are marked by the dashed lines. One of the most impressive features is that all three non-dust-season profiles show similar patterns, with maximum extinction coefficient close to the surface and nearly exponentially decreased with height. This type of aerosol profile is commonly seen for the boundary layer aerosols [Ramanathan *et al.*, 2001]. On the contrary, the aerosol profiles in dust season are more complex, presenting multiple peaks above the planetary boundary layers. By subtracting the non-dust-season aerosol profiles from the dust season profile, the contribution of background aerosols can be eliminated. The residual signal highlighted by the gray shadow in Figure 7 is due to the excess occurrence of mineral dust during the dust season, which is regarded to be the real distribution of dust plumes. It is clearly seen that during the periods of investigation (dust season), dust plumes are elevated into the free troposphere with the single peak around 4 km over AS and SC. In contrast, the dust plume over YS presents more multilayered complex structure rather than the single-layered distribution, with relatively small magnitude of extinction coefficient around 4 km.

[30] The elevated dust plume over SC in the summer was described in detail by Prospero and Carlson [1981]. The bare desert surface is heated strongly during summer time and results in an extremely unstable and highly developed thermal mixing layer. During vertical mixing, dust particles are lifted into the free troposphere [Carlson and Prospero, 1972; Tindale and Pease, 1999]. When the hot, dry, and stable dusty air moves offshore blown by the easterly winds, it is undercut by the cool, moist maritime air and confined between two inversion layers around 850 hPa and 500 hPa, respectively [Prospero and Carlson, 1981]. Similar mechanism can be applied to AS for the elevated single layer dust plume. The multilayer structure of the dust plume over YS was claimed to be associated with different contributions from two major dust sources over east Asia, i.e., the Gobi desert and the Taklamakan Desert [Sun *et al.*, 2001]. Using long term climatological records of dust storms and meteorological data in China, Sun *et al.* concluded that mineral dust originating from the Gobi Desert cannot be lifted to altitudes higher than 3 km, while dust particles raised from the Taklamakan Desert are able to be entrained to the upper troposphere and can be transported over long distance. The combination of these two dust sources might result in a multiple layered structure for the east Asian dust plume.

#### 3.5.2. Comparison With Published Dust Profiles

[31] The elevated layer structure of dust plumes has been observed directly by many field experiments [Dulac and Chazette, 1998]. The Saharan dust plume was characterized by the aircraft measurements during Barbados Oceanographic and Meteorological Experiment (BOMEX) [Prospero and Carlson, 1972] and SHADE [Highwood *et al.*, 2003]. Dust profiles were also documented by the lidar observations in PRIDE [Colarco *et al.*, 2003b], ACE-2 [Welton *et al.*, 2000], and Surface of the Ocean, Fluxes and

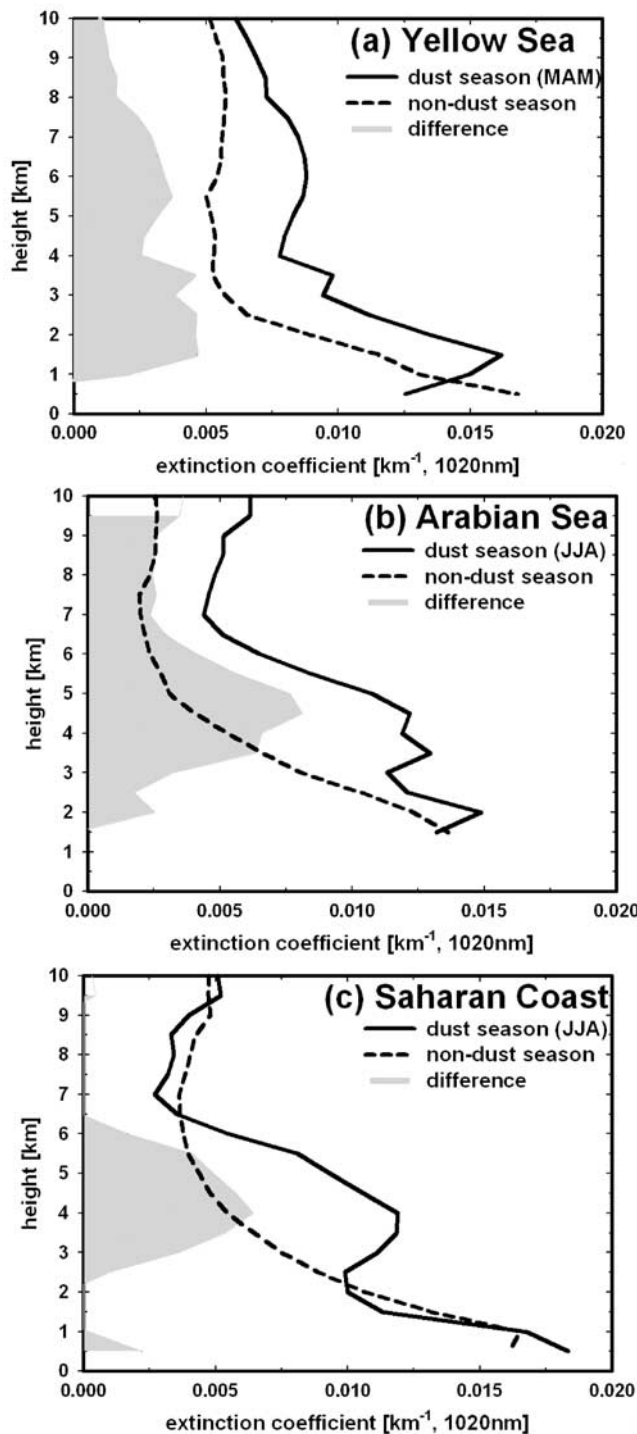


**Figure 7.** Vertical distribution of aerosol extinction coefficients ( $\text{km}^{-1}$ ) at 1020 nm measured from SAGE II (1981–2001 excluding volcanic years) for dust season (solid line), non-dust-season (dashed line), and the differences (gray shaded area) over (a) YS, (b) AS, and (c) SC.

Interactions with the Atmosphere/Atlantic Stratocumulus Transition Experiment (SOFIA/ASTEX) [Chazette et al., 1997]. Over the Mediterranean, field measurements reported that the stable Saharan layer was situated above

the trade wind marine boundary layer [Hamonou et al., 1997; Hamonou and Chazette, 1998; Pérez et al., 2006; Mattis et al., 2002; Müller et al., 2003; di Sarra et al., 2001].

[32] Over the north Indian Ocean, the top of the dust layer over the southwest monsoon region was found to reach a height range from 400 hPa during summer to 600 hPa during late spring and early fall [Ackerman and Cox, 1989]. Lidar observations accompanied with the backward trajectory analysis in the study of Müller et al. [2001] during INDOEX [Ramanathan et al., 2001] demonstrated that aerosols below 2500 m were solely from the pristine Indian Ocean with sea salt and sulfate aerosols as the major components, while the elevated aerosol layer with large backscatter and extinction coefficient at  $\sim 3800$  m altitude was proved to be the dust layer originating from the Arabian Peninsula and Somali region.

[33] Numerous observations over east Asia [Sasano, 1996; Liu et al., 2002; Zhou et al., 2002; Murayama et al., 2004, 2001; Shimizu et al., 2004] have shown the elevated dust plumes in the free troposphere during spring time. Kwon et al. [1997] revealed that air masses between 2 km and 4 km height mainly come from the Gobi Desert, while air parcels between 4 km and 7 km were originated from the region near the Taklamakan Desert. On the basis of aircraft observation, ground-based lidar measurements, and backward trajectory analysis, Matsuki et al. [2003] claimed that Taklamakan Desert is an important source for the background dust in the upper troposphere above 4 km. The airborne measurements during ACE-Asia also detected multiple aerosol layers near Tokyo [Murayama et al., 2003], which are the planetary boundary layer with fine aerosols from surface to  $\sim 1.2$ – $1.5$  km, an upper layer above  $\sim 3.5$  km dominated by dust particles, and an intermediate layer in between with the mixture of dust and fine aerosols. By means of Raman lidar observations at Nagoya ( $35.1^\circ\text{N}$ ,  $137.0^\circ\text{E}$ ), Sakai et al. [2000] found that the vertically integrated aerosol backscattering coefficients showed two peaks in spring, one is within the height range from 2 km to 4 km, another is between 4 km to 8 km. Murayama et al. [2001] coordinated a ground-based lidar network to observe the east Asian dust and highlighted the existence of a thin dust layer in the higher troposphere. Because dust particles can act as ice nuclei for cirrus clouds, the presence of uplifted dust particles in the upper troposphere may imply a potential indirect effect [DeMott et al., 2003; Sassen et al., 2003].

[34] To validate the dust profile derived from this study, we compared the SAGE II dust profiles with previous published observations. All the altitude-dependent parameters were normalized with respect to their maximum values to get the dimensionless signal based on the following equation:

$$F(h) = \frac{Ext(h)}{Ext_{\max}}, \quad (2)$$

where  $F(h)$  is the normalized signal ranging from zero to one as a function of height,  $Ext(h)$  is the measured profile with individual unit,  $Ext_{\max}$  is the maximum value of the measured profile. The normalization method cannot only maintain the original pattern of the aerosol profile, but also

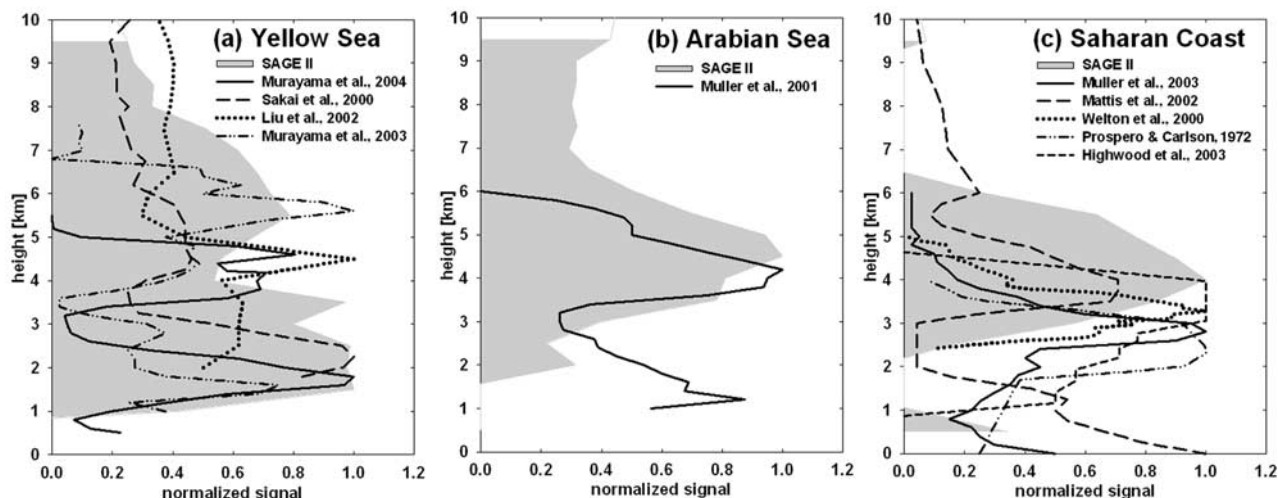


**Figure 8.** Comparison of dust vertical distribution between SAGE II (gray shaded area) and previous observations (lines) over (a) YS, (b) AS, and (c) SC.

make the comparison more feasible. The comparisons of the normalized dust profiles are showed in Figure 8. For YS (Figure 8a), most observations presented multiple dust layers except the lidar backscatter signal derived from the study of *Liu et al.* [2002], which exhibits a single dust layer with a peak at  $\sim 4$  km. The varying profiles from different field observations indicate that the vertical structure of the dust plume over east Asia is very complex. Owing to the scarcity of observations in the summer time over AS, only one lidar profile [*Müller et al.*, 2001] is available for the comparison (Figure 8b). Although the peak level of the lidar observation is slightly lower than what we found from SAGE II data, they both detected the elevated dust layer in the midtroposphere. The second peak at  $\sim 1$  km height observed by lidar was tracked to be the maritime aerosols by the trajectory analysis [*Müller et al.*, 2001]. Over SC (Figure 8c), all published profiles presented the elevated aerosol vertical structure with the peak level between 2 km and 4 km. The upper boundary of dust plume derived from SAGE II is slightly higher than the previous observations, which might come from the average method used in our study. However, the varieties of dust vertical profiles from individual lidar and aircraft observation do imply there is great diversity of dust vertical structure. It is worth noting that lidar and aircraft measurements could have more local effects owing to the limitation of observation period and covering area, while SAGE II represents the climatological vertical distribution of the dust plumes over large region with a decadal timescale. In spite of the uncertainty of SAGE II aerosol extinction coefficient data, the consistence between SAGE II profiles and previous findings in the literature confirms the reliability of SAGE II data to detect the elevated dust plumes. In the following sections, the elevated dust profiles derived from SAGE II are used to retrieve the radiative forcing caused by mineral dust.

#### 4. Radiative Impacts

[35] In this study, the direct radiative forcing of dust aerosols is under consideration, which is defined as the difference of net radiative flux (downward minus upward

flux) ( $\text{W m}^{-2}$ ) with dust and without dust. The TOA radiative forcing represents the warming/cooling effect on the whole atmosphere-Earth system induced by mineral dust, while the surface forcing is limited to the Earth surface only. The difference between the TOA forcing and the surface forcing represents the flux change within the atmosphere. The atmospheric flux changes are used to calculate the heating rate changes ( $\text{K/day}$ ) by dust. Seasonal averaged MODIS AOD data (2000–2004) and GOCART dust fraction (2001) are combined to derive the optical depth of dust aerosols. Both SW and LW radiative forcing are calculated for the three target regions (YS, AS, and SC) under the clear- and all-sky conditions.

##### 4.1. Clear-Sky Dust Forcing

[36] Figure 9 illustrated the geographic distributions of seasonal mean SW and LW dust forcing ( $\text{W m}^{-2}$ ) at the ocean surface over three target regions. The patterns of both SW (Figures 9a, 9c, and 9e) and LW (Figures 9b, 9d, and 9f) dust forcing follow the regional distribution of dust AOD, with highest forcing near the coastline and gradually decreasing toward the remote ocean. It is clearly seen that the SW dust effect at the ocean surface is cooling everywhere, while the LW forcing adds energy to the ocean surface. That is because dust particles both scatter and absorb the incoming solar radiation, both of these processes lead to the reduction of the SW flux reaching the dark ocean surface, which is also called the surface dimming. Dust particles also absorb the outgoing terrestrial flux emitted from the ocean surface and underlying atmosphere, and reemit the IR flux in all directions. The downward part of the emitted LW flux adds energy to the ocean surface. However, the magnitude of LW forcing is fairly small compared to the strong SW cooling. The largest LW warming is  $\sim 15 \text{ W m}^{-2}$  over SC, while the strongest SW cooling to the ocean surface is larger than  $-55 \text{ W m}^{-2}$  over AS.

[37] Dust forcing efficiency ( $\text{W m}^{-2} \tau^{-1}$ ), defined as the rate of change of radiative forcing per unit increase in dust AOD [*Ramanathan et al.*, 2001], is derived from the slope of the dust radiative forcing with respect to dust AOD,

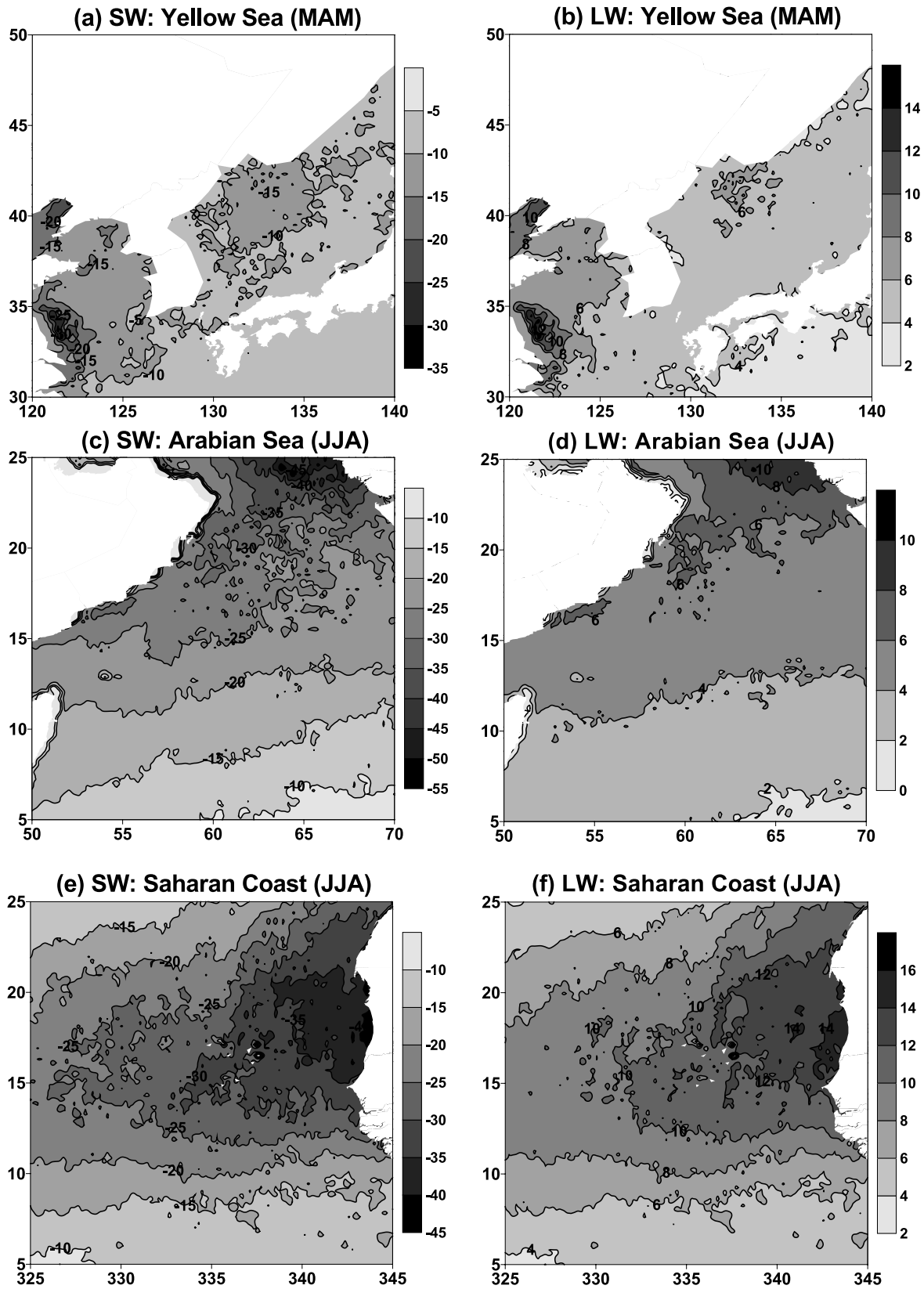
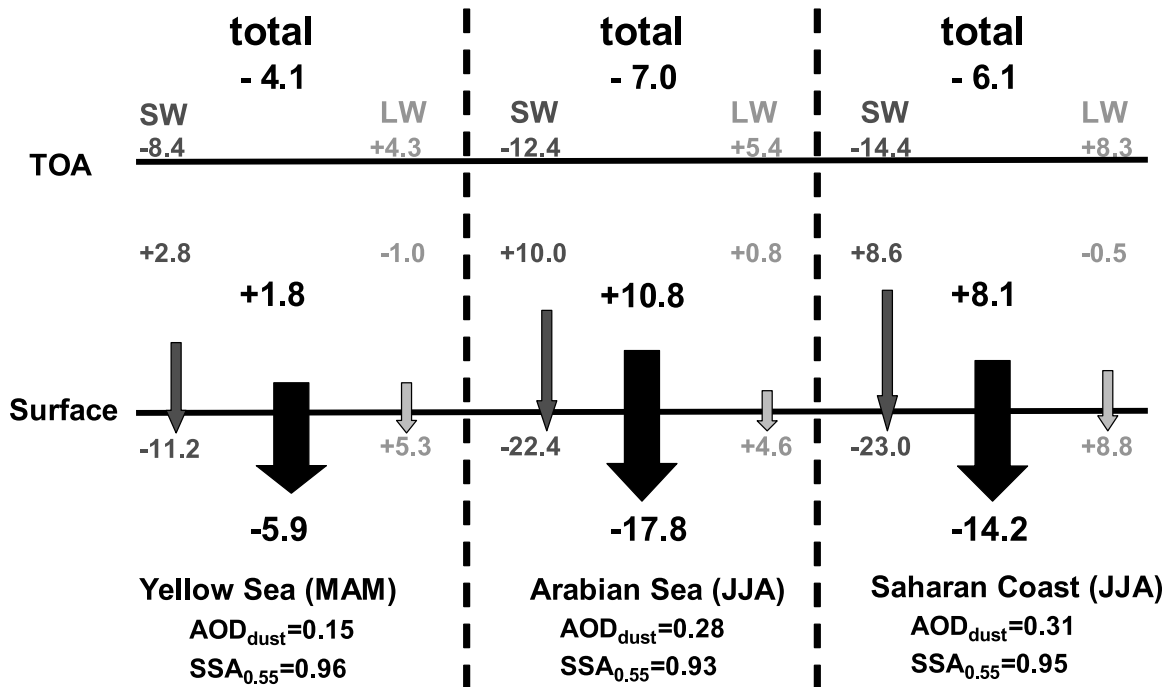


Figure 9. Clear-sky seasonal mean SW (a, c, e) and LW (b, d, f) dust forcing ( $W m^{-2}$ ) at the surface over YS (a, b), AS (c, d), and SC (e, f).



**Figure 10.** Clear-sky regional and seasonal mean SW, LW, and total (SW + LW) radiative forcing ( $\text{W m}^{-2}$ ) by dust plumes.

which is an effective method for comparison of aerosol forcing among different studies. The SW dust forcing efficiency ( $\text{W m}^{-2} \tau^{-1}$ ) at TOA (surface) is  $-43.7$  ( $-63.7$ ),  $-42.1$  ( $-78.3$ ),  $-41.1$  ( $-69.5$ ) for YS, AS, and SC, respectively. However, the LW dust forcing efficiency at TOA (surface) is relatively smaller, only  $+25.5$  ( $+31.8$ ),  $+18.1$  ( $+15.4$ ), and  $+22.8$  ( $+24.7$ )  $\text{W m}^{-2} \tau^{-1}$  over YS, AS, and SC, respectively. The prior study by *Li et al.* [2004] estimated the TOA and surface forcing efficiencies for the Saharan dust to be  $-35 \pm 3$  and  $-65 \text{ W m}^{-2} \tau^{-1}$ , respectively. It is important to note that *Li et al.*'s TOA forcing was obtained from satellite radiation budget studies. The retrieved model values in this study are consistent with *Li et al.*'s [2004] values.

[38] Processes involved in the radiative interactions with dust particles are illustrated in Figure 10 for the clear-sky conditions. Owing to the nonuniform distributions of dust plumes in both spatial and timescales, the regional and seasonal averaged dust optical depths are relatively small, which are 0.15 for YS, 0.28 for AS, and 0.31 for SC at 550 nm. The SW radiative forcing by dust is negative both at TOA and at the surface. The magnitude of surface forcing is much larger than the TOA forcing because of the large absorption of solar radiation by the atmosphere, noting that the atmosphere flux change equals TOA forcing minus surface forcing. The strongest SW forcing occurs over AS, although the regional and seasonal mean dust AOD over AS is smaller than that over SC. The fairly strong absorption ( $\text{SSA} \sim 0.93$  at 550 nm) of Arabian dust is the main reason for the strong SW forcing. On the contrary, the magnitude of LW TOA forcing is comparable to that of LW surface forcing, which leads to very small effect of LW forcing in the atmosphere. Although the positive LW forcing can compensate about half of the negative SW

forcing at TOA, the total dust forcing (SW + LW) is still dominated by the SW forcing; that is, dust plume has a negative forcing on the Earth-atmosphere system. As shown in Figure 10, the total dust radiative forcing over AS is the largest among the three regions and the total forcing over YS is the minimum, the atmospheric absorption over YS only accounts for  $\sim 20\%$  of the atmospheric absorption over AS.

[39] Although large differences of the selected region and observation period between this study and others make a direct comparison difficult, the results presented here are comparable to the values reported in prior studies. The ACE-Asia reported  $-5.5$  and  $-9.3 \text{ W m}^{-2}$  forcing at TOA and surface, respectively, for the mineral dust ( $\text{SSA} \sim 0.98$ ) over the east Asia ( $20^\circ\text{N}$ – $50^\circ\text{N}$ ,  $100^\circ\text{E}$ – $150^\circ\text{E}$ ) during 5–15 April 2001 [*Seinfeld et al.*, 2004]. The PRIDE campaign [*Christopher et al.*, 2003] assessed the diurnal mean SW dust forcing at TOA and surface to be  $-12.3 \pm 9.6$  and  $-18.1 \pm 15.8 \text{ W m}^{-2}$  in the Puerto Rico region during summer months. LW forcing values explored in our study are in the range of the IR dust forcing reported by *Sokolik et al.* [1998], which are  $\sim 2$ – $7 \text{ W m}^{-2}$  at TOA and  $\sim 7$ – $14 \text{ W m}^{-2}$  at surface for background conditions over arid or semiarid regions.

[40] The SW, LW and net (SW + LW) dust heating rate under clear-sky conditions are shown by the dashed lines in Figure 11. Mineral dust absorbs the incoming solar radiation and enhances heating of the layer where dust plumes exist. The absorption along with the scattering cuts down the incoming solar flux thus decreasing the heating rates of the air below the dust layer (Figure 11a). The maximum SW dust heating is located in the midtroposphere over AS with the value about 0.5 K/day. The heating rate over YS is very small (less than 0.15 K/day for the peak) owing to strong

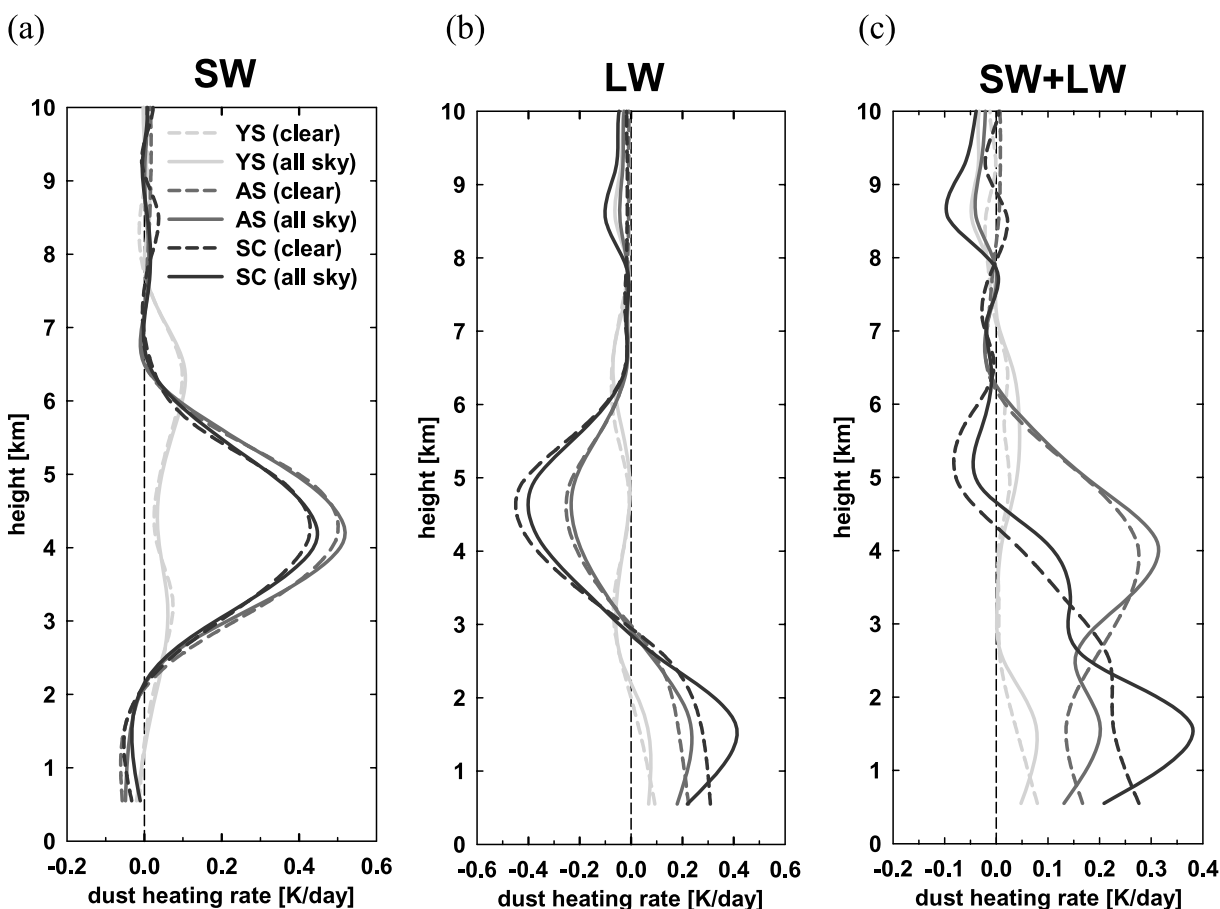


**Figure 11.** Regional and seasonal mean dust heating rate (K/day) under clear sky (dashed line) and all sky (solid line) for (a) SW, (b) LW, and (c) total (SW + LW).

scattering, which is in the range of  $\sim 0.08\text{--}0.4$  K/day estimated by *Nakajima et al.* [1989] for the east Asian yellow sand. On the contrary, the LW effect (Figure 11b) of the dust plumes enhances the LW cooling of the free troposphere because the upward and downward emissions of the LW flux by the dust is larger than the absorbed LW radiation. The net effect is energy loss inside the dust layer. One of the important features in Figure 11b is the strong LW warming below the base of the dust layer. That is because the elevated dust plumes increase downwelling LW flux and enhance the atmospheric absorption in the lower atmosphere.

[41] It is seen that SW (Figure 11a) and LW (Figure 11b) dust heating rates are determined by the vertical structure of the dust plumes, while total dust heating rate (Figure 11c) is more complex because of the counteracting effects between SW and LW. Over YS, total dust heating rate is the smallest among three regions, the maximum warming is less than 0.1 K/day as a result of the small dust optical depth, strong scattering properties, and multiple layered vertical structure. As to the dust plume over AS, the SW warming inside the dust layer is approximately twice the LW cooling, so the total heating rate change over AS is positive from the surface to  $\sim 6$  km, with maximum warming inside the dust layer centered at  $\sim 4$  km. Although the vertical profile over SC is similar to that over AS, the total heating rate change of Saharan dust has a different pattern, with maximum

warming near the surface, gradually decreasing with altitude, and turning to negative heating rate above  $\sim 4$  km.

#### 4.2. All-Sky Dust Forcing

[42] We reran the MACR model with seasonally averaged cloud fraction and cloud optical depth derived from ISCCP data. The dust radiative forcing under all-sky conditions is compared with that under clear sky as listed in Table 3. The occurrence of clouds reduces dust radiative forcing both in SW and in LW. The reduction of SW TOA forcing is nearly equivalent to the reduction of surface forcing with a value of about  $\sim 5\text{--}7$   $\text{W m}^{-2}$ , which implies a negligible change in the atmospheric absorption ( $< 0.3$   $\text{W m}^{-2}$ ) owing to the competing effects by different clouds. For instance, the existence of low clouds over the dark ocean increases the surface albedo thus enhancing the SW absorption by the elevated dust layer, while high clouds block the incoming solar flux and result in less absorption by dust aerosols. Thus the net effect of clouds on the atmospheric absorption induced by dust plumes is quite small. The weakening of the LW dust forcing by clouds is fairly mild, and the maximum difference between all sky and clear sky is less than 2  $\text{W m}^{-2}$ .

[43] Even though the occurrence of clouds results in a small change to the atmospheric absorption, dust heating rate can be affected greatly by clouds, especially for the LW heating rate (Figure 11b). The warming below the dust layer

**Table 3.** Comparison of Dust Radiative Forcing Between Clear-Sky and All-Sky Conditions Over Yellow Sea, Arabian Sea, and Saharan Coast<sup>a</sup>

Region	Sky Condition	Top of the Atmosphere			Surface			Atmospheric Absorption		
		SW	LW	Total	SW	LW	Total	SW	LW	Total
YS	All	-3.24	+3.18	-0.06	-6.01	+4.11	-1.9	+2.76	-0.93	+1.83
	Clear	-8.36	+4.31	-4.05	-11.17	+5.3	-5.87	+2.81	-0.99	+1.82
AS	All	-6.37	+4.63	-1.74	-16.31	+3.84	-12.47	+9.94	+0.79	+10.73
	Clear	-12.41	+5.41	-7.0	-22.36	+4.56	-17.8	+9.96	+0.85	+10.81
SC	All	-6.91	+7.21	+0.3	-15.87	+7.01	-8.86	+8.96	+0.2	+9.16
	Clear	-14.37	+8.3	-6.07	-23.03	+8.8	-14.23	+8.66	-0.5	+8.16

<sup>a</sup>Units for dust radiative forcing are  $\text{W m}^{-2}$ .

under all-sky conditions (solid lines in Figure 11) is greatly enhanced mainly because low clouds absorb more LW flux emitted from the upper dust layer than clear sky, which results in the excess warming in the cloud layer. The change of the SW dust heating rate by clouds is fairly small compared with its influence on the LW effect. As shown by the solid lines in Figure 11a, the SW dust heating rates under all sky are similar to the clear-sky conditions, except that the warming inside the dust layer increases slightly and the cooling below the dust layer weakens by within 0.1 K/day. The total dust heating rates under all sky are mainly affected by the LW effect of clouds. Overall, the low-level clouds have been found to have a strong effect on dust heating rate change, especially causing additional warming below the dust layer. As discussed by *Prospero and Carlson* [1981], stratiform clouds are always found in the marine boundary layer under the elevated dust layer, which implies more complex interactions of dust plumes with clouds.

## 5. Consideration of Other Factors

[44] Although the results for dust direct radiative forcing are valid for oceanic regions in clear-sky and all-sky conditions, conclusions would differ over land regions, especially for the SW TOA radiative forcing. This is because the surface reflectance is much higher over land than over the ocean. The occurrence of dust layer over the dark ocean surface increases the planetary albedo and enhances the outgoing SW flux at TOA, thus causes large negative SW TOA forcing. However, over the land region, the magnitude of negative TOA forcing can be reduced and even the sign can be changed from negative to positive because the elevated dust layer can trap part of the outgoing SW flux reflected by the bright surface, thus the energy loss at TOA is reduced. The detailed discussion of uncertainties of SW radiative forcing with respect to surface albedo can be found from the studies by *Claquin et al.* [1998] and *Liao and Seinfeld* [1998]. The LW radiative forcing by mineral dust is a strong function of the surface temperature which presents far greater diurnal variation over land compared with oceans. For example, *Haywood et al.* [2005] showed that the TOA LW forcing of mineral dust could reach  $+50 \text{ W m}^{-2}$  at local noon over hot desert surfaces. However, this issue is beyond the scope of this paper.

[45] Although this study attempt to minimize errors by relying on much observational parameters for model input to estimate dust radiative forcing, the results have some unavoidable uncertainties coming from the input parameters, such as MODIS AOD, dust AOD fraction and SSA. As

discussed by *Remer et al.* [2002], the uncertainty of MODIS AOD over the ocean is about  $\pm 0.05$ . The sensitivity test in this study showed that this MODIS AOD uncertainty can lead to about 12% to 33% uncertainty to total dust radiative forcing. The application of GOCART dust AOD fraction is another possible source of error. If MODIS large-mode AOD ratio were used, dust AOD will increase 10% over YS, and decrease about 7% and 38% over AS and SC, respectively. The change of dust AOD by using MODIS large-mode AOD ratio will further bring about 2% to 37% uncertainty to the calculated dust forcing. The other major uncertainty of the estimated dust forcing arises from SSA. A  $\pm 0.03$  uncertainty of AERONET SSA [*Dubovik et al.*, 2000] can lead to about 12% uncertainty in the SW TOA forcing. The largest error caused by SSA uncertainty lies in the atmospheric absorption with maximum uncertainty of about 90% over YS. Although the aforementioned three parameters have large effects to the calculated dust radiative forcing, the pattern of dust heating rate is not affected, only the magnitude of dust heating rate changes with the range from 0.04 to 0.2 K/day, where SSA was found to have the largest effect in regulating the magnitude of dust heating rate.

[46] Dust vertical profile can also bring uncertainties to the estimated forcing. Owing to the scarce of SAGE II data at the level close to the Earth surface, the boundary layer aerosol signals might be filtered by SAGE II retrieval technique. To test the uncertainty of boundary dust aerosols on dust radiative forcing, exponentially decreased profiles extending from ocean surface to the base of the elevated dust layer was added to the SAGE II dust profile. The sensitivity tests showed that the inclusion of boundary dust aerosols causes 1% to 17% uncertainty of TOA forcing, 3% to 17% uncertainty of surface forcing, and 15% to 50% uncertainty of atmospheric absorption. The occurrence of boundary layer dust aerosol has large effect on both the pattern and the magnitude of dust heating rate. Large change of heating rate pattern was found near the boundary layer, where SW heating rate switched from slight cooling to slight warming and the magnitude of LW warming decreased owing to the energy loss from these boundary layer dust aerosols. Inside the elevated dust layers, the magnitudes of both SW warming and LW cooling were diminished. The overall change in the magnitude of the total dust heating rate change is within 0.1 K/day. Although applications of the SAGE II data for description of dust vertical profiles reveal encouraging results, it is recommended that a comprehensive data comparison analysis should be conducted by using tropospheric measurements from

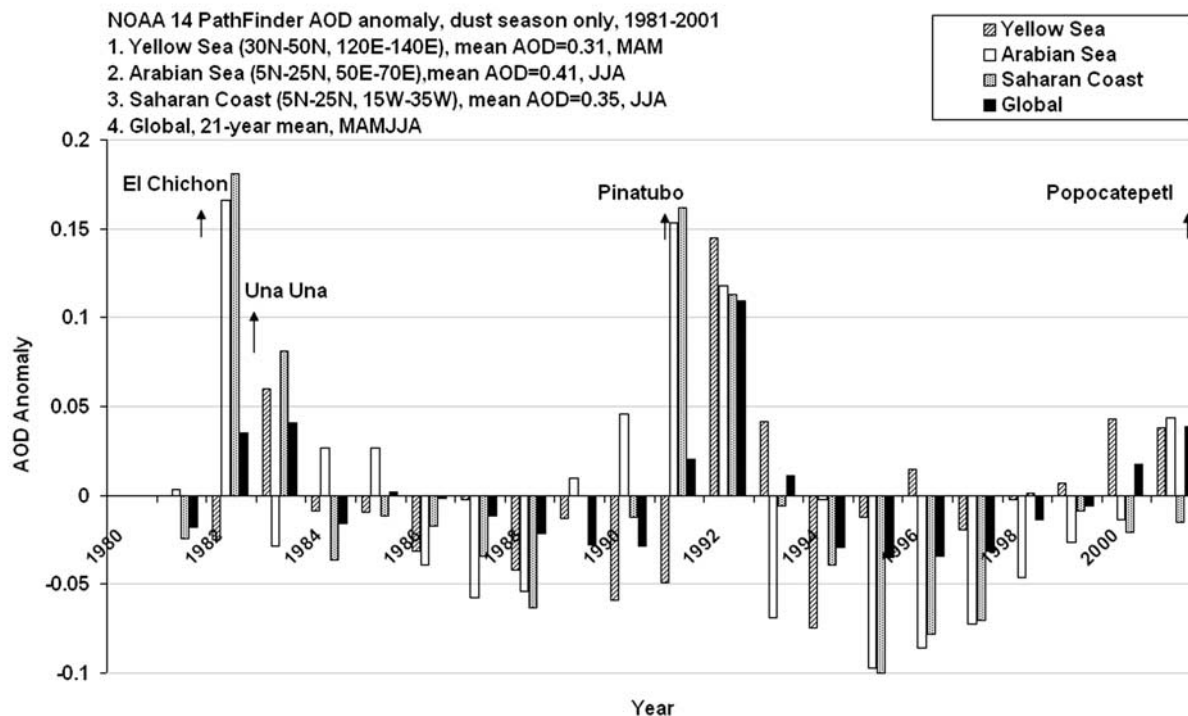


**Figure 12.** AOD anomalies from 1981 to 2001 in the dust seasons over YS, AS, and SC. Global mean AOD anomaly is also shown for comparison.

different instruments. Observations by Ice, Cloud, Land Elevation Satellite (ICESat) with the space-based lidar started since January 2003 can provide a valuable data set to perform cross check with SAGE II for the dust vertical profiles on a climatological basis.

[47] The satellite data exhibits considerable variability on decadal timescales. As displayed in Figure 12, the volcanic eruptions bring large amount of aerosol particles and cause the greatest positive anomalies even only the dust season was considered. The maximum AOD anomaly was 0.18 for the Saharan Coast and 0.17 for the Arabian Sea, occurring in 1982 when the El Chichon erupted; the maximum AOD anomaly for Yellow Sea was 0.14, appearing in 1992, a year after the Pinatubo eruption; and the maximum global mean anomaly was found in the second year of Pinatubo with a value of 0.11. Despite being shadowed by the volcanic eruption, an increasing trend of AOD anomaly can be defined clearly from the mid-1990s to early this century. The transition from negative anomalies to positive anomalies during dust season deserves some concerns since it may imply the increasing trend of dust emission in recent decade. The historical study over China by Zhou and Zhang [2003] also showed an increasing trend of severe dust events in China from late 1990s. More observations and model studies are required to better understand the trend of dust plumes.

[48] In this study, mineral dust was simplified to be externally mixed with other aerosol species, that is, dust particles are suspended in the air individually and have no interaction with other aerosol particles. Field observations and laboratory experiments suggest that dust particles can be mixed with sulfate, organic carbon, and sea salt aerosols

[Iwasaka *et al.*, 2003; Andreae *et al.*, 1986; Zhang *et al.*, 2003a; Song *et al.*, 2005; Clarke *et al.*, 2004; Zhang *et al.*, 2003b]. For example, the SSA during dust season is about 0.91 at AERONET Beijing site, which is the downstream of anthropogenic pollutions. In contrast, in the upstream desert site Dunhuang, larger SSA ( $\sim 0.96$ ) was observed in the same period. However, it is presently difficult to define the fraction of the “polluted” dust particles and the “unpolluted” dust particles. According to Jacobson [2001], absorption of solar radiation is greatly enhanced if the aerosol particle is accompanied by black carbon. Thus the radiative forcing estimated in this study may underestimate the SW effect of dust plumes. In a future paper, we will combine more observations to investigate the radiative impacts of the dust-soot mixtures. Another issue requiring further research is the assessment of the radiative impact by the anthropogenic dust particles, such as those due to agricultural activity and land-surface changes etc. On the basis of the model estimation by Tegen *et al.* [1996], about  $\sim 30$ – $50\%$  mineral dust particles are associated with the anthropogenic sources. Although great efforts have been made to evaluate the radiative impacts of anthropogenic dust, large uncertainties still exist in estimating the fraction of manmade dust particles.

## 6. Summary and Conclusions

[49] Through the analysis of long-term AVHRR AOD data sets, the climatological distributions of three major dust plumes spreading over the Pacific, Indian, and Atlantic oceans during last 2 decades were examined. Distinct dust seasons have been identified to be March–April–May for

the dust plume over the Pacific Ocean, and June–July–August for those over the Indian Ocean and the Atlantic Ocean. The transport patterns as well as the geographic distribution of dust plumes gradually declining from the source continent to the remote oceans were clearly illustrated. By subtracting the non-dust-season profile from the dust season SAGE II aerosol profile, we were able to determine the layer-like structures of the dust plumes showing high concentrations in the free troposphere. An elevated single dust layer was found above marine boundary layer with peak around 4 km over AS and SC, and multilayered structure of dust plumes were found over YS. The agreement of the dust profiles between SAGE II and lidar and aircraft observations implied that our findings are consistent with previous studies. Large-mode MODIS AOD data are analyzed to show the annual cycle of the coarse-mode particles. The comparison with GOCART dust fraction demonstrated that MODIS large-mode AOD ratio might have uncertainty to accurately estimate the contribution of dust particles relatively to total AOD.

[50] Direct radiative forcing of dust plumes was estimated by Monte Carlo radiative transfer model. Although LW warming compensated part of SW cooling, SW forcing dominates the total effect of dust plumes with negative TOA forcing everywhere over the ocean. The dust plume over AS causes the largest forcing among the three dust plumes, with the clear-sky regional and seasonal mean net forcing to be  $-7.0 \text{ W m}^{-2}$  and  $-17.8 \text{ W m}^{-2}$  at the TOA and ocean surface, respectively. The large flux divergence between the TOA forcing and surface forcing results in the largest atmospheric heating over AS, with the clear-sky atmospheric heating to be  $+10.8 \text{ W m}^{-2}$ . The atmospheric absorption induced by dust plume over YS was the smallest ( $<2 \text{ W m}^{-2}$ ) because of the small dust AOD (fraction) and strong SW scattering.

[51] The atmospheric heating rate changes by dust depend on the vertical distribution of the dust plumes under the clear sky. Large SW heating was found inside the dust layer due to strong absorption of the incoming solar radiation, with the maximum heating to be around  $+0.5 \text{ K/day}$  over AS and centered at  $\sim 4 \text{ km}$  where dust concentration peaks. The LW effect results in a strong cooling throughout the dust layer with the maximum cooling located just above the dust peak level and moderate heating below the dust layer. Dust plumes over SC exert the maximum LW effect on heating rates, with up to  $-0.5 \text{ K/day}$  LW cooling in the free troposphere and about  $+0.3 \text{ K/day}$  warming in the boundary layer. The net heating rate by the dust plumes is the sum of the SW and the LW heating rates. Over SC, large LW cooling inside the dust layer offsets up to 80% SW heating and results in about  $-0.1 \text{ K/day}$  net heating rate change at the height  $\sim 5 \text{ km}$  over SC. Over AS, the net heating rate change is dominated by SW heating because the maximum LW cooling is less than 60% of the SW heating, which leads to  $+0.3 \text{ K/day}$  net heating inside the dust layer and moderate heating below the dust base. The net heating rate change over YS is the smallest among the three regions, with magnitude within  $0.1 \text{ K/day}$ . The occurrence of clouds masked the effect of dust plumes by reducing the forcing both at TOA and at the surface; however, the heating rate change in all sky showed little difference from clear sky except that the LW warming below the dust layer was

enhanced by low-level clouds. The strong radiative forcing by dust plumes over the oceans implies further impacts on the hydrological cycle, atmospheric stability, and global cloud coverage.

[52] This study is motivated by the urgent need to fully understand the climate impacts of dust plumes over the worldwide oceans. By investigating the climatological distribution and direct radiative forcing of three major dust plumes over the Pacific, Indian, and Atlantic oceans, we would like to stimulate more profound studies to reveal the impacts of dust particles on the cloud formation, general circulation, and water budget.

[53] **Acknowledgments.** The MODIS AOD data come from NASA GSFC Distributed Active Archive Center, and the SAGE II data come from NASA Langley Research Center. The authors thank Shane Mattoo for her help in the MODIS AOD format. We are thankful to the anonymous reviewers for their helpful comments and constructive suggestions that have resulted in improvements of this manuscript. This study was partially funded by the National Science Foundation (NSF) through grant ATM 9612887, and by NASA NAS1-98141.

## References

- Ackerman, S. A., and S. K. Cox (1989), Surface weather observations of atmospheric dust over the southwest summer monsoon region, *Meteorol. Atmos. Phys.*, *41*, 19–34.
- Andreae, M. O., R. J. Charlson, F. Bruynseels, H. Storms, R. Van Grieken, and W. Maenhaut (1986), Internal mixtures of sea salt, silicates and excess sulfate in marine aerosols, *Science*, *232*, 1620–1623.
- Antuña, J. C., A. Robock, G. L. Stenchikov, L. W. Thomason, and J. E. Barnes (2002), Lidar validation of SAGE II aerosol measurements after the 1991 Mount Pinatubo eruption, *J. Geophys. Res.*, *107*(D14), 4194, doi:10.1029/2001JD001441.
- Bellouin, B., O. Boucher, J. Haywood, and S. Reddy (2005), Global estimates of aerosol direct radiative forcing from satellite measurements, *Nature*, *438*, 1138–1141.
- Carlson, T. N., and S. G. Benjamin (1980), Radiative heating rates for Saharan dust, *J. Atmos. Sci.*, *37*, 193–213.
- Carlson, T. N., and J. M. Prospero (1972), The large scale movement of Saharan air outbreaks over the northern equatorial Atlantic, *J. Appl. Meteorol.*, *11*, 283–297.
- Chazette, P., J. Pelon, C. Moulin, V. Trouillet, I. Carrasco, F. Dulac, W. Guelle, P. Bousquet, and P. H. Flamant (1997), Synergy between lidar and Meteosat measurements for a Saharan dust event during SOFIA/ASTEX, *J. Aerosol Sci.*, *28*, S659–S660.
- Chin, M., et al. (2002), Tropospheric aerosol optical thickness from the GOCART model and comparisons with satellite and Sun photometer measurements, *J. Atmos. Sci.*, *59*, 461–483.
- Christopher, S. A., J. Wang, Q. Ji, and S. Tsay (2003), Estimation of diurnal shortwave dust aerosol radiative forcing during PRIDE, *J. Geophys. Res.*, *108*(D19), 8596, doi:10.1029/2002JD002787.
- Chu, D. A., Y. J. Kaufman, C. Ichoku, L. A. Remer, D. Tanré, and B. N. Holben (2002), Validation of MODIS aerosol optical depth retrieval over land, *Geophys. Res. Lett.*, *29*(12), 8007, doi:10.1029/2001GL013205.
- Chun, Y., and J. Y. Lim (2004), The recent characteristics of Asian Dust and haze events in Seoul, Korea, *Meteorol. Atmos. Phys.*, *87*, 143–152.
- Chung, C. E., V. Ramanathan, D. Kim, and I. A. Podgorny (2005), Global anthropogenic aerosol direct forcing derived from satellite and ground-based observations, *J. Geophys. Res.*, *110*, D24207, doi:10.1029/2005JD006356.
- Claquin, T., M. Schulz, Y. J. Balkanski, and O. Boucher (1998), Uncertainties in assessing radiative forcing by mineral dust, *Tellus, Ser. B*, *50*, 491–505.
- Clarke, A. D., et al. (2004), Size distributions and mixtures of dust and black carbon aerosol in Asian outflow: Physiochemistry and optical properties, *J. Geophys. Res.*, *109*, D15S09, doi:10.1029/2003JD004378.
- Clough, S. A., F. X. Kneizys, and R. W. Davies (1989), Line shape and the water vapor continuum, *Atmos. Res.*, *23*, 229–241.
- Colarco, P. R., et al. (2003a), Saharan dust transport to the Caribbean during PRIDE: 2. Transport, vertical profiles, and deposition in simulations of in situ and remote sensing observations, *J. Geophys. Res.*, *108*(D19), 8590, doi:10.1029/2002JD002659.
- Colarco, P. R., O. B. Toon, and B. N. Holben (2003b), Saharan dust transport to the Caribbean during PRIDE: 1. Influence of dust sources and removal mechanisms on the timing and magnitude of downwind aerosol

- optical depth events from simulations of in situ and remote sensing observations, *J. Geophys. Res.*, *108*(D19), 8589, doi:10.1029/2002JD002658.
- d'Almeida, G. A., and L. Schütz (1983), Number, mass and volume distributions of mineral aerosols and soils of Sahara, *J. Clim. Appl. Meteorol.*, *22*, 233–243.
- DeMott, P. J., K. Sassen, M. R. Poellot, D. Baumgardner, D. C. Rogers, S. D. Brooks, A. J. Prenni, and S. M. Kreidenweis (2003), African dust aerosols as atmospheric ice nuclei, *Geophys. Res. Lett.*, *30*(14), 1732, doi:10.1029/2003GL017410.
- Diner, D. J., W. A. Abdou, C. J. Bruegge, J. E. Conel, K. A. Crean, B. J. Gaitley, M. C. Helmlinger, R. A. Kahn, J. V. Martonchik, and S. H. Pforz (2001), MISR aerosol optical depth retrievals over southern Africa during the SAFARI-2000 dry season campaign, *Geophys. Res. Lett.*, *28*, 3127–3130.
- di Sarra, A., T. Di Iorio, M. Cacciani, G. Fiocco, and D. Fuà (2001), Saharan dust profiles measured by lidar at Lampedusa, *J. Geophys. Res.*, *106*, 10,335–10,348.
- Dubovik, O., A. Smirnov, B. N. Holben, M. D. King, Y. J. Kaufman, and I. Slutsker (2000), Accuracy assessments of aerosol optical properties retrieved from AERONET Sun and sky radiance measurements, *J. Geophys. Res.*, *105*, 9791–9806.
- Dubovik, O., B. N. Holben, T. F. Eck, A. Smirnov, Y. J. Kaufman, M. D. King, D. Tanre, and I. Slutsker (2002), Variability of absorption and optical properties of key aerosol types observed in worldwide locations, *J. Atmos. Sci.*, *59*, 590–608.
- Duce, R. A. (1995), Sources, distributions, and fluxes of mineral aerosols and their relationship to climate, in *Aerosol Forcing of Climate*, edited by R. J. Charlson and J. Heintzenberg, pp. 43–72, Wiley, New York.
- Dulac, F., and P. Chazette (1998), Balloonborne profiling of African dust over the tropical Atlantic, *J. Aerosol Sci.*, *29*, S1265–S1266.
- Eck, T. F., et al. (2005), Columnar aerosol optical properties at AERONET sites in central eastern Asia and aerosol transport to the tropical mid-Pacific, *J. Geophys. Res.*, *110*, D06202, doi:10.1029/2004JD005274.
- Fu, Q., and K. N. Liou (1992), On the correlated k-distribution method for radiative transfer in nonhomogeneous atmospheres, *J. Atmos. Sci.*, *49*, 2139–2156.
- Ginoux, P., M. Chin, I. Tegen, J. Prospero, B. Holben, O. Dubovik, and S. J. Lin (2001), Sources and distributions of dust aerosols simulated with the GOCART model, *J. Geophys. Res.*, *106*, 20,255–20,273.
- Gong, S. L., X. Zhang, T. Zhao, I. G. Mckendry, D. A. Jaffe, and N. Lu (2003), Characterization of soil dust aerosol in China and its transport and distribution during 2001 ACE-Asia: 2. Model simulation and validation, *J. Geophys. Res.*, *108*(D9), 4262, doi:10.1029/2002JD002633.
- Goody, R. M., R. West, L. Chen, and D. Crisp (1989), The correlated k-distribution method for radiation calculations in nonhomogeneous atmospheres, *J. Quant. Spectrosc. Radiat. Transfer*, *42*, 539–550.
- Hamonou, E., and P. Chazette (1998), Evidence of Saharan mineral aerosols transport to the Mediterranean inside well-defined layers, *J. Aerosol Sci.*, *29*, S1263–S1264.
- Hamonou, E., P. Chazette, A. Papayannis, D. Balis, F. Marengo, V. Santacesaria, and G. Ancellet (1997), Ground-based measurements of Saharan dust optical properties in the frame of the European MEDUSE Project, *J. Aerosol Sci.*, *28*, S695–S696.
- Harrison, S. P., K. E. Kohfeld, C. Roelandt, and T. Claquin (2001), The role of dust in climate changes today, at the Last Glacial Maximum and in the future, *Earth Sci. Rev.*, *54*, 43–80.
- Haywood, J., P. Francis, S. Osborne, M. Glew, N. Loeb, E. Highwood, D. Tanré, G. Myhre, P. Formenti, and E. Hirst (2003), Radiative properties and direct radiative effect of Saharan dust measured by the C-130 aircraft during SHADE: 1. Solar spectrum, *J. Geophys. Res.*, *108*(D18), 8577, doi:10.1029/2002JD002687.
- Haywood, J. M., R. P. Allan, I. Culverwell, T. Slingo, S. Milton, J. Edwards, and N. Clerbaux (2005), Can desert dust explain the outgoing longwave radiation anomaly over the Sahara during July 2003?, *J. Geophys. Res.*, *110*, D05105, doi:10.1029/2004JD005232.
- Highwood, E. J., J. M. Haywood, M. D. Silverstone, S. M. Newman, and J. P. Taylor (2003), Radiative properties and direct effect of Saharan dust measured by the C-130 aircraft during Saharan Dust Experiment (SHADE): 2. Terrestrial spectrum, *J. Geophys. Res.*, *108*(D18), 8578, doi:10.1029/2002JD002552.
- Holben, B. N., et al. (1998), AERONET: A federated instrument network and data archive for aerosol characterization, *Remote. Sens. Environ.*, *66*, 1–16.
- Huang, J., B. Lin, P. Minnis, T. Wang, X. Wang, Y. Hu, Y. Yi, and J. K. Ayers (2006), Satellite-based assessment of possible dust aerosols semi-direct effect on cloud water path over east Asia, *Geophys. Res. Lett.*, *33*, L19802, doi:10.1029/2006GL026561.
- Husar, R. B., et al. (2001), Asian dust events of April 1998, *J. Geophys. Res.*, *106*, 18,317–18,330.
- Ichoku, C., D. A. Chu, S. Mattoo, Y. J. Kaufman, L. A. Remer, D. Tanré, I. Slutsker, and B. N. Holben (2002), A spatio-temporal approach for global validation and analysis of MODIS aerosol products, *Geophys. Res. Lett.*, *29*(12), 8006, doi:10.1029/2001GL013206.
- Intergovernmental Panel on Climate Change (IPCC) (2001), *Climate Change 2001, Contribution of Working Group I to the Third Assessment Report of the Intergovernmental Panel on Climate Change*, 881 pp., Cambridge Univ. Press, New York.
- Iwasaka, Y., et al. (2003), Importance of dust particles in the free troposphere over the Taklamakan Desert: Electron microscopic experiments of particles collected with a balloonborne particle impactor at Dunhuang, China, *J. Geophys. Res.*, *108*(D23), 8644, doi:10.1029/2002JD003270.
- Jacobson, M. Z. (2001), Strong radiative heating due to the mixing state of black carbon in atmospheric aerosols, *Nature*, *409*, 695–697.
- Kato, S., T. P. Ackerman, J. H. Mather, and E. E. Clothiaux (1999), The k-distribution method and correlated-k approximation for a shortwave radiative transfer model, *J. Quant. Spectrosc. Radiat. Transfer*, *62*, 109–121.
- Kaufman, Y. J., D. Tanré, O. Dubovik, A. Karnieli, and L. A. Remer (2001), Absorption of sunlight by dust as inferred from satellite and ground-based remote sensing, *Geophys. Res. Lett.*, *28*, 1479–1482.
- Kaufman, Y. J., I. Koren, L. A. Remer, D. Tanré, P. Ginoux, and S. Fan (2005), Dust transport and deposition observed from the Terra-Moderate Resolution Imaging Spectroradiometer (MODIS) spacecraft over the Atlantic Ocean, *J. Geophys. Res.*, *110*, D10S12, doi:10.1029/2003JD004436.
- Kent, G. S., C. R. Trepte, K. M. Skeens, and D. M. Winker (1998), LITE and SAGE II measurements of aerosols in the Southern Hemisphere upper troposphere, *J. Geophys. Res.*, *103*, 19,111–19,128.
- Kent, G. S., C. R. Trepte, P. H. Wang, and P. L. Lucker (2003), Problems in separating aerosol and cloud in the Stratospheric Aerosol and Gas Experiment (SAGE) II data set under conditions of lofted dust: Application to the Asian deserts, *J. Geophys. Res.*, *108*(D14), 4410, doi:10.1029/2002JD002412.
- Kwon, S. A., Y. Iwasaka, T. Shibata, and T. Sakai (1997), Vertical distribution of atmospheric particles and water vapor densities in the free troposphere: Lidar measurement in spring and summer in Nagoya, Japan, *Atmos. Environ.*, *31*, 1459–1465.
- Lacis, A. A., and V. Oinas (1991), A description of the correlated k distribution method for modeling nongray gaseous absorption, thermal emission, and multiple scattering in vertically inhomogeneous atmospheres, *J. Geophys. Res.*, *96*, 9027–9063.
- Lau, K. M., M. K. Kim, and K. M. Kim (2006), Asian summer monsoon anomalies induced by aerosol direct forcing: The role of the Tibetan Plateau, *Clim. Dyn.*, *26*, 855–864.
- Li, F., and V. Ramanathan (2002), Winter to summer monsoon variation of aerosol optical depth over the tropical Indian Ocean, *J. Geophys. Res.*, *107*(D16), 4284, doi:10.1029/2001JD000949.
- Li, F., A. M. Vogelmann, and V. Ramanathan (2004), Saharan dust aerosol radiative forcing measured from space, *J. Clim.*, *17*(13), 2558–2571.
- Liao, H., and J. H. Seinfeld (1998), Radiative forcing by mineral dust aerosols: Sensitivity to key variables, *J. Geophys. Res.*, *103*, 31,637–31,645.
- Liu, Z., N. Sugimoto, and T. Murayama (2002), Extinction-to-backscatter ratio of Asian dust observed with high-spectral-resolution lidar and Raman lidar, *Appl. Opt.*, *41*, 2760–2767.
- Lunt, D. J., and P. J. Valdes (2002), The modern dust cycle: Comparison of model results with observations and study of sensitivities, *J. Geophys. Res.*, *107*(D23), 4669, doi:10.1029/2002JD002316.
- Mahowald, N. M., D. R. Muhs, S. Levis, P. J. Rasch, M. Yoshioka, C. S. Zender, and C. Luo (2006), Change in atmospheric mineral aerosols in response to climate: Last glacial period, preindustrial, modern, and doubled carbon dioxide climates, *J. Geophys. Res.*, *111*, D10202, doi:10.1029/2005JD006653.
- Marchuk, G., G. Mikhailov, M. Nazarahev, R. Darbinjan, B. Kargin, and B. Elepov (1980), *The Monte Carlo Methods in Atmospheric Optics*, Springer-Verlag, New York.
- Martins, J. V., D. Tanré, L. Remer, Y. Kaufman, S. Mattoo, and R. Levy (2002), MODIS cloud screening for remote sensing of aerosol over oceans using spatial variability, *Geophys. Res. Lett.*, *29*(12), 8009, doi:10.1029/2001GL013252.
- Matsuki, A., et al. (2003), Seasonal dependence of the long-range transport and vertical distribution of free tropospheric aerosols over east Asia: On the basis of aircraft and lidar measurements and isentropic trajectory analysis, *J. Geophys. Res.*, *108*(D23), 8663, doi:10.1029/2002JD003266.
- Mattis, I., A. Ansmann, D. Müller, U. Wandinger, and D. Althausen (2002), Dual-wavelength Raman lidar observations of the extinction-to-backscatter ratio of Saharan dust, *Geophys. Res. Lett.*, *29*(9), 1306, doi:10.1029/2002GL014721.
- Mbourou, G. N., J. J. Bertrand, and S. E. Nicholson (1997), The diurnal and seasonal cycles of wind-born dust over Africa north of the equator, *J. Appl. Meteorol.*, *36*, 868–882.

- Meloni, D., A. D. Sarra, T. D. Iotio, and G. Fiocco (2005), Influence of the vertical profile of Saharan dust on the visible direct radiative forcing, *J. Quant. Spectrosc. Radiat. Transfer*, *93*, 413–497.
- Müller, D., K. Franke, F. Wagner, D. Althausen, A. Ansmann, J. Heintzenberg, and G. Verver (2001), Vertical profiling of optical and physical particle properties over the tropical Indian Ocean with six-wavelength lidar: 2. Case studies, *J. Geophys. Res.*, *106*, 28,577–28,596.
- Müller, D., I. Mattis, U. Wandinger, A. Ansmann, D. Althausen, O. Dubovik, S. Eckhardt, and A. Stohl (2003), Saharan dust over a central European EARLINET-AERONET site: Combined observations with Raman lidar and Sun photometer, *J. Geophys. Res.*, *108*(D12), 4345, doi:10.1029/2002JD002918.
- Murayama, T., et al. (2001), Ground-based network observation of Asian dust events of April 1998 in east Asia, *J. Geophys. Res.*, *106*, 18,345–18,360.
- Murayama, T., et al. (2003), An intercomparison of lidar-derived aerosol optical properties with airborne measurements near Tokyo during ACE-Asia, *J. Geophys. Res.*, *108*(D23), 8651, doi:10.1029/2002JD003259.
- Murayama, T., D. Müller, K. Wada, A. Shimizu, M. Sekiguchi, and T. Tsukamoto (2004), Characterization of Asian dust and Siberian smoke with multi-wavelength Raman lidar over Tokyo, Japan in spring 2003, *Geophys. Res. Lett.*, *31*, L23103, doi:10.1029/2004GL021105.
- Myhre, G., A. Grini, J. M. Haywood, F. Stordal, B. Chatenet, D. Tanré, J. K. Sundet, and I. S. A. Isaksen (2003), Modeling the radiative impact of mineral dust during the Saharan Dust Experiment (SHADE) campaign, *J. Geophys. Res.*, *108*(D18), 8579, doi:10.1029/2002JD002566.
- Nakajima, T., M. Tanaka, M. Yamano, M. Shiobara, K. Arao, and Y. Nakanishi (1989), Aerosol optical characteristics in the yellow sand events observed in May, 1982 in Nagasaki, part II: Model, *J. Meteorol. Soc. Jpn.*, *67*, 279–291.
- Pease, P. P., V. P. Tchakerian, and N. W. Tindale (1998), Aerosols over the Arabian Sea: Geochemistry and source areas for aeolian desert dust, *J. Arid Environ.*, *39*, 477–496.
- Penner, J. E., et al. (2001), Aerosols, their direct and indirect effects, in *Climate Change 2001: The Scientific Basis. Contribution of Working Group I to the Third Assessment Report of the Intergovernmental Panel on Climate Change*, edited by J. Houghton et al., pp. 289–348, Cambridge Univ. Press, New York.
- Pérez, C., S. Nickovic, J. M. Baldasano, M. Sicard, F. Rocadenbosch, and V. E. Cachorro (2006), A long Saharan dust event over the western Mediterranean: Lidar, Sun photometer observations, and regional dust modeling, *J. Geophys. Res.*, *111*, D15214, doi:10.1029/2005JD006579.
- Perlwitz, J., I. Tegen, and R. L. Miller (2001), Interactive soil dust aerosol model in the GISS GCM: 1. Sensitivity of the soil dust cycle to radiative properties of soil dust aerosols, *J. Geophys. Res.*, *106*, 18,167–18,192.
- Podgorny, I. A., and V. Ramanathan (2001), A modeling study of the direct effect of aerosols over the tropical Indian Ocean, *J. Geophys. Res.*, *106*, 24,097–24,106.
- Podgorny, I. A., A. M. Vogelmann, and V. Ramanathan (1998), Effects of cloud shape and water vapor distribution on solar absorption in the near infrared, *Geophys. Res. Lett.*, *25*, 1899–1902.
- Prospero, J. M., and T. N. Carlson (1972), Vertical and areal distribution of Saharan dust over the western equatorial North Atlantic ocean, *J. Geophys. Res.*, *77*, 5255–5265.
- Prospero, J. M., and T. N. Carlson (1981), Saharan air outbreaks over the tropical North Atlantic, *Pure Appl. Geophys.*, *119*, 677–691.
- Prospero, J. M., P. Ginoux, O. Torres, S. E. Nicholson, and T. E. Gill (2002), Environmental characterization of global sources of atmospheric soil dust identified with the NIMBUS 7 Total Ozone Mapping Spectrometer (TOMS) absorbing aerosol product, *Rev. Geophys.*, *40*(1), 1002, doi:10.1029/2000RG000095.
- Raes, F., T. Bates, F. Mcgovern, and M. Van-Liedekerke (2000), The 2nd aerosol characterization experiments (ACE-2) general overview and main results, *Tellus, Ser. B*, *52*, 111–125.
- Ramanathan, V., et al. (2001), Indian ocean experiment: An integrated analysis of the climate forcing and effects of the great Indo-Asian haze, *J. Geophys. Res.*, *106*, 28,371–28,398.
- Remer, L. A., et al. (2002), Validation of MODIS aerosol retrieval over ocean, *Geophys. Res. Lett.*, *29*(12), 8008, doi:10.1029/2001GL013204.
- Reynolds, R. W., N. A. Rayner, T. M. Smith, D. C. Stokes, and W. Wang (2002), An improved in situ and satellite SST analysis for climate, *J. Clim.*, *15*, 1609–1625.
- Rossow, W. B., and R. A. Schiffer (1999), Advances in understanding clouds from ISCCP, *Bull. Am. Meteorol. Soc.*, *80*, 2261–2288.
- Rossow, W. B., A. W. Walker, D. E. Beusichel, and M. D. Roiter (1996), *International Satellite Cloud Climatology Project (ISCCP) Documentation of New Cloud Datasets*, WMO/TD-737, 115 pp., World Meteorol. Org., Geneva.
- Rothman, L. S., et al. (2003), The HITRAN molecular spectroscopic database: Edition of 200 0 including updates through 2001, *J. Quant. Spectrosc. Radiat. Transfer*, *82*, 5–44.
- Sakai, T., T. Shibata, S. A. Kwon, Y. S. Kim, K. Tamura, and Y. Iwasaka (2000), Free tropospheric aerosol backscatter, depolarization ratio, and relative humidity measured with the Raman lidar at Nagoya in 1994–1997: Contributions of aerosols from the Asian Continent and the Pacific Ocean, *Atmos. Environ.*, *34*, 431–442.
- Sasano, Y. (1996), Tropospheric aerosol extinction coefficient profiles derived from scanning lidar measurements over Tsukuba, Japan from 1990 to 1993, *Appl. Opt.*, *35*(24), 4941–4952.
- Sassen, K., P. J. DeMott, J. M. Prospero, and M. R. Poellot (2003), Saharan dust storms and indirect aerosol effects on clouds: CRYSTAL-FACE results, *Geophys. Res. Lett.*, *30*(12), 1633, doi:10.1029/2003GL017371.
- Satheesh, S. K., V. Ramanathan, Xu Li-Jones, J. M. Lobert, I. A. Podgorny, J. M. Prospero, B. N. Holben, and N. G. Loeb (1999), A model for the natural and anthropogenic aerosols over the tropical Indian Ocean derived from Indian Ocean Experiment data, *J. Geophys. Res.*, *104*, 27,421–27,440.
- Seinfeld, J. H., et al. (2004), Regional climatic and atmospheric chemical effects of Asian dust and pollution, *Bull. Am. Meteorol. Soc.*, *85*(3), 367–380.
- Shao, Y. P., et al. (2003), Northeast Asian dust storms: Real-time numerical prediction and validation, *J. Geophys. Res.*, *108*(D22), 4691, doi:10.1029/2003JD003667.
- Shi, G., H. Wang, B. Wang, S. Gong, T. Zhao, W. Li, and T. Aoki (2005), Sensitivity experiments on the effects of optical properties of dust aerosols on their radiative forcing under sky condition, *J. Meteorol. Soc. Jpn.*, *83A*, 333–346.
- Shimizu, A., N. Sugimoto, I. Matsui, K. Arao, I. Uno, T. Murayama, N. Kagawa, K. Aoki, A. Uchiyama, and A. Yamazaki (2004), Continuous observations of Asian dust and other aerosols by polarization lidars in China and Japan during ACE-Asia, *J. Geophys. Res.*, *109*, D19S17, doi:10.1029/2002JD003253.
- Sirocko, F. (1991), Deep-sea sediments of the Arabian Sea: A paleoclimatic record of the southwest-Asian summer monsoon, *Geol. Rundsch.*, *80*, 557–566.
- Sokolik, I. N., and O. B. Toon (1999), Incorporation of mineralogical composition into models of the radiative properties of mineral aerosol from UV to IR wavelengths, *J. Geophys. Res.*, *104*, 9423–9444.
- Sokolik, I. N., A. Andronova, and T. C. Johnson (1993), Complex refractive index of atmospheric dust aerosols, *Atmos. Environ.*, *27*, 2495–2502.
- Sokolik, I. N., O. B. Toon, and R. W. Bergstrom (1998), Modeling the radiative characteristics of airborne mineral aerosols at infrared wavelengths, *J. Geophys. Res.*, *103*, 8813–8826.
- Sokolik, I. N., D. M. Winker, G. Bergametti, D. A. Gillette, G. Carmichael, Y. J. Kaufman, L. Gomes, L. Schuetz, and J. E. Penner (2001), Introduction to special section: Outstanding problems in quantifying the radiative impacts of mineral dust, *J. Geophys. Res.*, *106*, 18,015–18,028.
- Song, C. H., and G. R. Carmichael (2001), A three-dimensional modeling investigation of the evolution processes of dust and sea-salt particles in east Asia, *J. Geophys. Res.*, *106*, 18,131–18,154.
- Song, C. H., K. Meier, R. J. Weber, V. Kapustin, and A. Clarke (2005), Dust composition and mixing state inferred from airborne composition measurements during ACE-Asia C130 Flight #6, *Atmos. Environ.*, *39*, 359–369.
- Stowe, L. L., A. A. Ignatove, and R. R. Singh (1997), Development, validation and potential enhancements to the second generation operational aerosol product at NOAA/NESDIS, *J. Geophys. Res.*, *102*, 16,923–16,934.
- Stowe, L. L., H. Jacobowitz, G. Ohring, K. P. Knapp, and N. R. Nalli (2002), The Advanced Very High Resolution Radiometer (AVHRR) Pathfinder Atmosphere (PATMOS) climate dataset: Initial analyses and evaluations, *J. Clim.*, *15*(11), 1243–1260.
- Sun, J., M. Zhang, and T. Liu (2001), Spatial and temporal characteristics of dust storm in China and its surrounding regions, 1960–1999: Relations to source area and climate, *J. Geophys. Res.*, *106*, 10,325–10,333.
- Tanré, D., Y. J. Kaufman, M. Herman, and S. Mattoo (1997), Remote sensing of aerosol properties over oceans using the MODIS/EOS spectral radiances, *J. Geophys. Res.*, *102*, 16,971–16,988.
- Tanré, D., Y. J. Kaufman, B. N. Holben, B. Chatenet, A. Karnieli, F. Lavenu, L. Blarel, O. Dubovik, L. A. Remer, and A. Smirnov (2001), Climatology of dust aerosol size distribution and optical properties derived from remotely sensed data in the solar spectrum, *J. Geophys. Res.*, *106*, 18,205–18,217.
- Tanré, D., J. Haywood, J. Pelon, J. F. Léon, B. Chatenet, P. Formenti, P. Francis, P. Goloub, E. J. Highwood, and G. Myhre (2003), Measurement and modeling of the Saharan dust radiative impact: Overview of the Saharan Dust Experiment (SHADE), *J. Geophys. Res.*, *108*(D18), 8574, doi:10.1029/2002JD003273.
- Tegen, I., A. A. Lacis, and I. Fung (1996), The influence on climate forcing of mineral aerosols from disturbed soils, *Nature*, *380*, 419–422.

- Thomason, L. W., and G. Taha (2003), SAGE III aerosol extinction measurements: Initial results, *Geophys. Res. Lett.*, *30*(12), 1631, doi:10.1029/2003GL017317.
- Thomason, L. W., L. R. Poole, and T. R. Deshler (1997), A global climatology of stratospheric aerosol surface area density as deduced from SAGE II: 1984–1994, *J. Geophys. Res.*, *102*, 8967–8976.
- Tindale, N. W., and P. P. Pease (1999), Aerosols over the Arabian Sea: Atmospheric transport pathways and concentrations of dust and sea salt, *Deep Sea Res., Part II*, *46*, 1577–1595.
- Torres, O., P. K. Bhartia, J. R. Herman, Z. Ahmda, and J. Gleason (1998), Derivation of aerosol properties from satellite measurements of back-scattered ultraviolet radiation: Theoretical basis, *J. Geophys. Res.*, *103*, 17,099–17,110.
- Torres, O., P. K. Bhartia, J. R. Herman, A. Sinyuk, P. Gioux, and B. Holben (2002), A long-term record of aerosol optical depth from TOMS observations and comparison to AERONET measurements, *J. Atmos. Sci.*, *59*, 398–413.
- Twomey, S. A. (1977), The influence of pollution on the shortwave albedo of clouds, *J. Atmos. Sci.*, *34*, 1149–1152.
- Uppala, S. M., et al. (2005), The ERA-40 reanalysis, *Q. J. R. Meteorol. Soc.*, *131*, 2961–3012.
- Vogelmann, A. M., V. Ramanathan, and I. A. Podgorny (2001), Scale dependence of solar heating rates in convective cloud systems with implications to general circulation models, *J. Clim.*, *14*(N8), 1738–1752.
- Volz, F. E. (1973), Infrared optical constants of ammonium sulphate, Sahara dust, volcanic pumice and fly ash, *Appl. Opt.*, *12*, 564–567.
- Wang, P. H., G. S. Kent, R. E. Veiga, G. K. Yue, L. R. Poole, J. Fishman, and M. P. McCormick (1999), A model for identifying the aerosol-only mode of SAGE II 1.02- $\mu\text{m}$  extinction coefficient data at altitudes below 6.5 km, *J. Geophys. Res.*, *104*, 9609–9615.
- Welton, E. J., et al. (2000), Ground-based lidar measurements of aerosols during ACE-2: Instrument description, results, and comparisons with other ground-based and airborne measurements, *Tellus, Ser. B*, *52*, 636–651.
- Woodward, S. (2001), Modeling the atmospheric life cycle and radiative impact of mineral dust in the Hadley Centre climate model, *J. Geophys. Res.*, *106*, 18,155–18,166.
- Zender, C. S., H. Bian, and D. Newman (2003), Mineral Dust Entrainment and Deposition (DEAD) model: Description and 1990s dust climatology, *J. Geophys. Res.*, *108*(D14), 4416, doi:10.1029/2002JD002775.
- Zhang, D., J. Zang, G. Shi, Y. Iwasaka, A. Matsuki, and D. Trochkin (2003a), Mixture state of individual Asian dust particles at a coastal site of Qingdao, China, *Atmos. Environ.*, *37*, 3895–3901.
- Zhang, D., Y. Iwasaka, G. Shi, J. Zang, A. Matsuki, and D. Trochkin (2003b), Mixture state and size of Asian dust particles collected at southwestern Japan in spring 2000, *J. Geophys. Res.*, *108*(D24), 4760, doi:10.1029/2003JD003869.
- Zhou, Z., and G. Zhang (2003), Typical severe dust storms in northern China during 1954–2002, *Chin. Sci. Bull.*, *48*(21), 2366–2370.
- Zhou, J., G. Yu, C. Jin, F. Qi, D. Liu, H. Hu, Z. Gong, G. Shi, T. Nakajima, and T. Takamura (2002), Lidar observations of Asian dust over Hefei, China, in spring 2000, *J. Geophys. Res.*, *107*(D15), 4252, doi:10.1029/2001JD000802.

---

D. Kim, F. Li, V. Ramanathan, and A. Zhu, Center for Atmospheric Sciences, Scripps Institution of Oceanography, University of California, San Diego, 9500 Gilman Drive, La Jolla, CA 92093-0239, USA. (azhu@ucsd.edu)